energies

MDPI

Article

Engineering-Scale Integrated Energy System Data Projection Demonstration via the Dynamic Energy Transport and Integration Laboratory

Ramon Yoshiura *,†, Sarah Creasman † and Aaron Epiney

Idaho National Laboratory (INL), 2525 N. Fremont Ave., Idaho Falls, ID 83415, USA; sarah.creasman@inl.gov (S.C.); aaron.epiney@inl.gov (A.E.)

* Correspondence: ramon.yoshiura@inl.gov

† These authors contributed equally to this work.

Abstract: The objective of this study is to demonstrate and validate the Dynamic Energy Transport and Integration Laboratory (DETAIL) preliminary scaling analysis using Modelica language system-code Dymola. The DETAIL preliminary scaling analysis includes a multisystem integral scaling package between thermal-storage and hydrogen-electrolysis systems. To construct the system of scaled equations, dynamical system scaling (DSS) was applied to all governing laws and closure relations associated with the selected integral system. The existing Dymola thermal-energy distribution system (TEDS) facility and high-temperature steam electrolysis (HTSE) facility models in the Idaho National Laboratory HYBRID repository were used to simulate a test case and a corresponding scaled case for integrated system HYBRID demonstration and validation. The DSS projected data based on the test-case simulations and determined scaling ratios were generated and compared with scaled case simulations. The preliminary scaling analysis performance was evaluated, and scaling distortions were investigated based on data magnitude, sequence, and similarity. The results indicated a necessity to change the normalization method for thermal storage generating optimal operating conditions of 261 kW power and mass flow rate of 6.42 kg/s and the possibility of reselecting governing laws for hydrogen electrolysis to improve scaling predictive properties. To enhance system-scaling similarity for TEDS and HTSE, the requirement for scaling validation via physical-facility demonstration was identified.

Keywords: integrated energy system; thermal-storage system; high-temperature steam electrolysis; dynamical system scaling; scaling validation; data extrapolation

Citation: Yoshiura, R.; Creasman, S.; Epiney, A. Engineering-Scale Integrated Energy System Data Projection Demonstration via the Dynamic Energy Transport and Integration Laboratory. *Energies* **2023**, *16*, 5878. https://doi.org/10.3390/en16165878

Academic Editors: Alan Brent, Shuli Liu and Panpan Song

Received: 11 July 2023
Revised: 24 July 2023
Accepted: 4 August 2023
Published: 8 August 2023

1. Introduction

As the energy infrastructure diversifies, and in light of the new worldwide zero-carbon initiatives, integrated energy systems (IES) are a flexible solution to optimally dispatch energy [1]. To make a waste-free and adaptable energy infrastructure a reality, innovative energy production strategies and method of distribution are essential. This includes considering the local and global effects of coupled energy source utilities (electric and thermal) and the associated users. Examples of optimal control failure leading to catastrophic outcomes include Texas in 2021—where record-breaking low temperatures impaired electricity utilities while increasing power demand [2]—and Argentina in 2022, where unprecedented high temperatures partially disabled power production and triggered higher electricity demand to such an extent as to limit the water-purification system, affecting supply [3]. As fossil-fuel power utilities—those without the capability for carbon capture (e.g., direct-air capture systems [4]) to be at least carbon neutral—are decommissioned or replaced, and industrial processes converted to non-carbon-emitting sources for heat or other energy forms (such as steam), macro- and microgrids must adapt to the load-balance daily demand. Another crucial component of future conversions towards zero-carbon is an assessment of

commodities and product prices due to different process shifts, which can be assessed via techno-economic analyses. For this reason, it is increasingly important to build IES capabilities to account for variants, such as daily demand and seasonal changes, to successfully load balance and maximize profits for hour-ahead, day-ahead, or real-time markets [5].

To plan and analyze the effects of various IESs, Idaho National Laboratory's (INL's) IES program conducts research, development, and deployment activities to expand the role of nuclear-centered electric utilities beyond supporting the electricity grid. The expanded roles include supplying energy to various industrial, transportation, and energy-storage applications. The development of IESs may include multiple energy inputs (e.g., nuclear, renewable, and fossil with carbon capture), multiple energy users (e.g., grid consumers, industrial heat or electricity users, transportation-fuel users), and multiple energy-storage options (e.g., thermal, electrical, and chemical). For a complete overview and assessment of different IES combinations, ongoing techno-economic and modeling simulations are being conducted. For nuclear power plants, the following three dynamic energy transport system pathways are defined: (1) process heat production, (2) electricity production, and (3) hydrogen production [6]. Furthermore, the possible end-user spectra are set from petroleum refining, chemical manufacturing, and cement production to mining, carbon conversion, and desalination (the schematic pathway is shown in Figure 1).

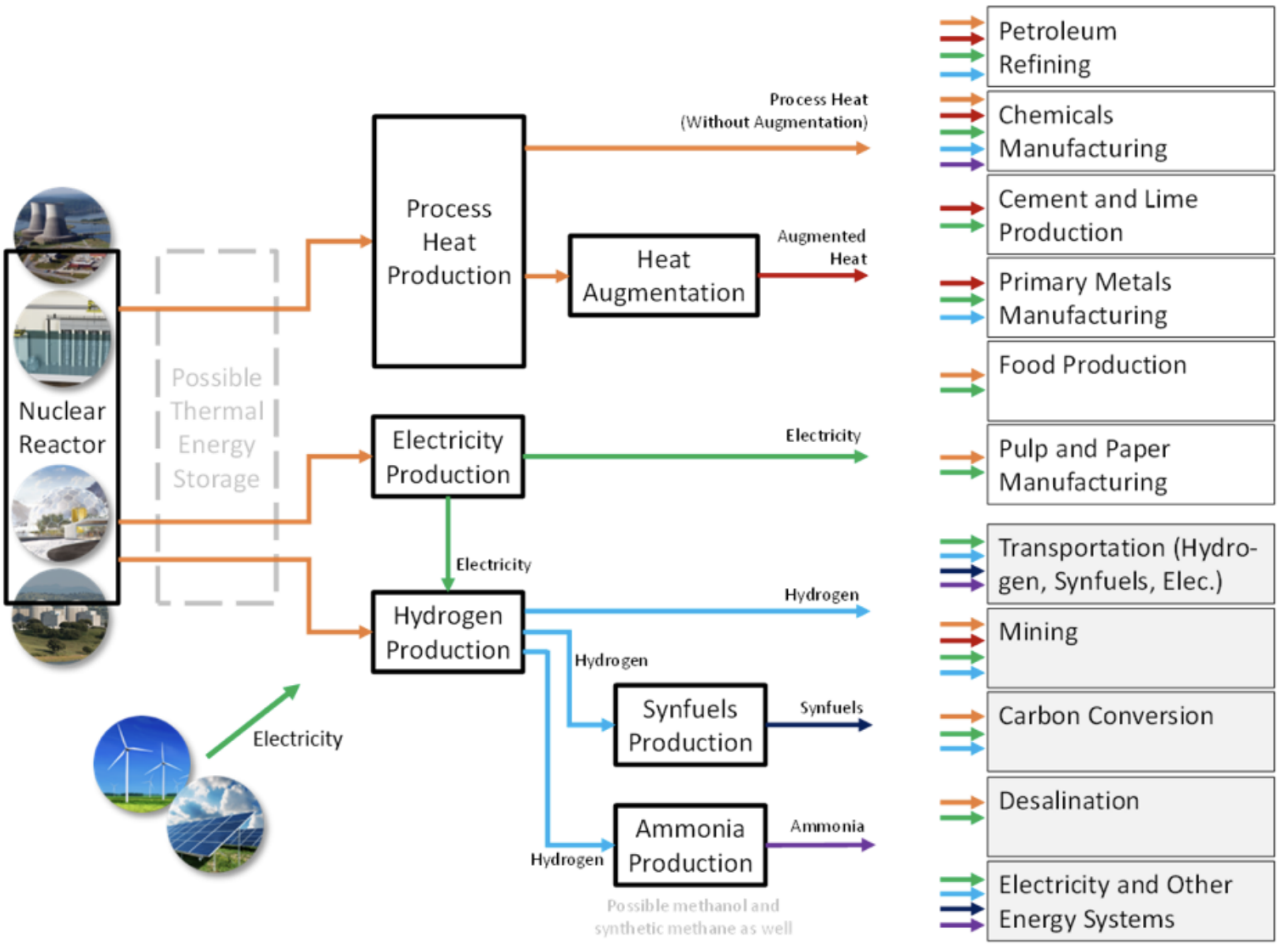

Figure 1. Potential industrial applications for direct electrical and thermal coupling with nuclear power [6].

The capability to emulate IES cases for various combinations is essential to measure the effectiveness and compatibility of one energy system to another. To demonstrate prospective interactive systems at the laboratory-scale, the Dynamic Energy Transport and Integration Laboratory (DETAIL) provides a combination of thermal storage, battery testing, hydrogen production, electric-vehicle charging, a digital real-time power grid,

distributed energy and microgrid power-plant operation, and a non-nuclear microreactor experimental testbed [1]. To expand DETAIL's emulation capabilities, interactions with external facilities are being planned, and real-time optimization tools are being developed within the Framework for Optimization of ResourCes and Economics (FORCE) code to make digital interactions possible. FORCE is a collection of software tools developed under the IES program to enable the analysis of the technical and economic viability of a myriad of IES configurations [7]. Within the framework, techno-economic assessments of the economic viability of grid-energy system configurations and transient-process modeling capabilities exist, accompanying soft and hard constraints to approach a short- or long-term optimized solution. One concern arises when interacting with external entities of different scales. Regardless of whether it is possible to digitally communicate in real time, inputs and outputs of different scales risk not characterizing either system. For this reason, system-to-system adapters for incoming and outgoing signals relative to DETAIL are required for data post-processing and conversion.

For thermal energy storage in particular, considering the current fleet and advanced nuclear power plant heat generation rates and standard four-hour storage capacity, storage systems such as two-tank molten salt, solid-media, and latent heat technologies are deemed well suited for the given different reactor sizes and operating temperatures [8]. For the given heat storage configuration shown in Figure 2, the nuclear reactor can operate at steady-state conditions at times of low electric demand, delay energy delivery, and enhance the capacity factor, enabling a faster return in capital costs.

IES cybersecurity resiliency is another assessment that is being addressed. Other national laboratories such as the National Renewable Energy Laboratory (NREL) are developing the design of cybersecurity emulations for energy systems, enabling exploration on how cyber–physical threats are identified to protect critical energy infrastructure, distributed energy resource systems, and data-driven communication networks [9]. Future collaborations with fellow national laboratory efforts are key to cover all aspects of IES.

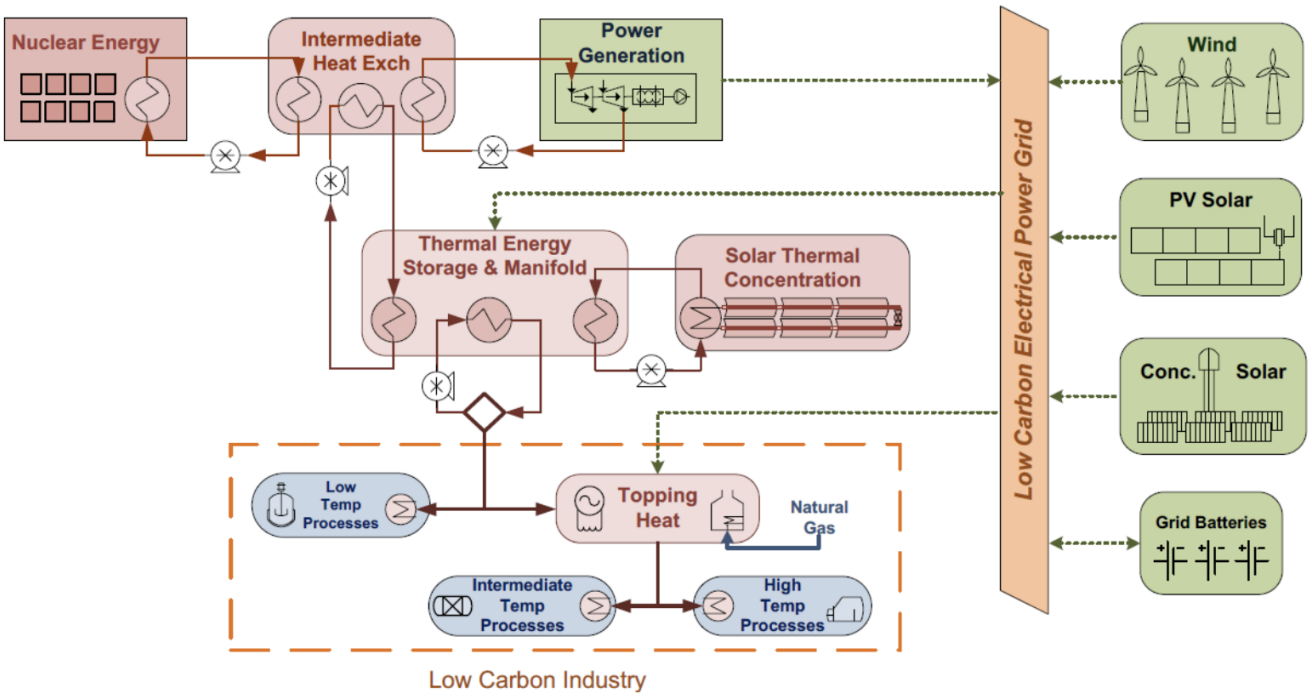

Figure 2. General architecture for thermally coupled IES [10].

As part two of this effort (part one is under [11,12]) to develop system-to-system adapters using scaling methodologies, the purposes of this continued effort are to:

1. Establish the framework to understand the requirements of how scaling ratios in one system will affect other connecting systems
2. Prepare and scale a demonstration case
3. Validate the scaling analysis via system code

In order to accomplish these particular efforts, a two-system scaling case—including interaction between the thermal energy distribution system (TEDS) facility and high temperature steam electrolysis (HTSE) facility—was selected. The scaling analysis should consider both top and bottom scaling to conserve the properties of each system. The selected validation tool is the Dynamic Modeling Laboratory (Dymola), a commercially available Modelica-based modeling and simulation environment for engineering applications [13,14]. The Dymola tool uses the Modelica modeling language [15], which has a causal connection of components governed by mathematical equations to facilitate modeling from first principles. Since modern scaling methodologies rely on and are based on first principles to determine the scaling relations among parameters of interest, the compatibility with the Modelica language is high and identifies Dymola as the primary candidate to conduct scaling validation. Specific models for TEDS and HTSE were developed prior to this research. Ideally, both models would be under the same simulation to demonstrate the two-system scaling effects. However, due to incomplete model enhancements, the Dymola framework connecting the TEDS and HTSE models remains under development. As an alternative, the TEDS and HTSE models will be run semi-coupled, where simulation conditions on the HTSE side will be based on TEDS-simulation feedback. After the scaled equations for both systems are derived and test-case simulations are available, the accelerated scaling ratios will be determined, and the projected data will be calculated. The scaled initial and boundary conditions will be implemented to Dymola models to generate an accelerated data set. By comparing the accelerated simulation data and the projected, scale-based data, the scaling efforts can be validated. In case scaling distortions are larger than anticipated, the cause will be investigated to improve current scaling analyses. If successful, the presented research will indicate the validity of utilizing dynamic scaling methods to anticipate changes in operating conditions, required configuration changes, and appropriate sizing of components based on the first principles and a similarity assessment. Although this method cannot replace design or experimental engineering, the information derived from the proposed research brings invaluable insights and justification to future IES architecture.

2. Facilities

2.1. TEDS Overview

The TEDS facility is a thermal-storage system in DETAIL specializing in thermal storage and discharge. The major components are (1) a therminol tank, (2) an oil–glycol heat exchanger, (3) a Chormalox heater, (4) a driving pump, (5) a thermocline thermal storage system (TTSS), and a steam generator (as shown in Figure 3 [16]).

Therminol-66, a high-performance, highly stable synthetic heat-transfer fluid, is circulated around the loop, acting as the main media providing thermal stability without forming volatile or highly viscous products between operating temperatures of −85° and 400 °C. This essentially allows accelerated heat transfer at or below atmospheric pressure, exhibiting a minimal difference in thermal conductivity at the specified operating temperatures (0.118 W/m·K–0.084 W/m·K). By injecting and ejecting heat via the Chromalox heater and oil–glycol heat exchanger, TEDS is segregated into two systems: (1) cold line and (2) hot line. The TTSS is strategically installed between the cold and hot lines as an alternate method to interchange fluids of different temperatures. To increase the thermal-storage capacity, an alumina filler is added [1].

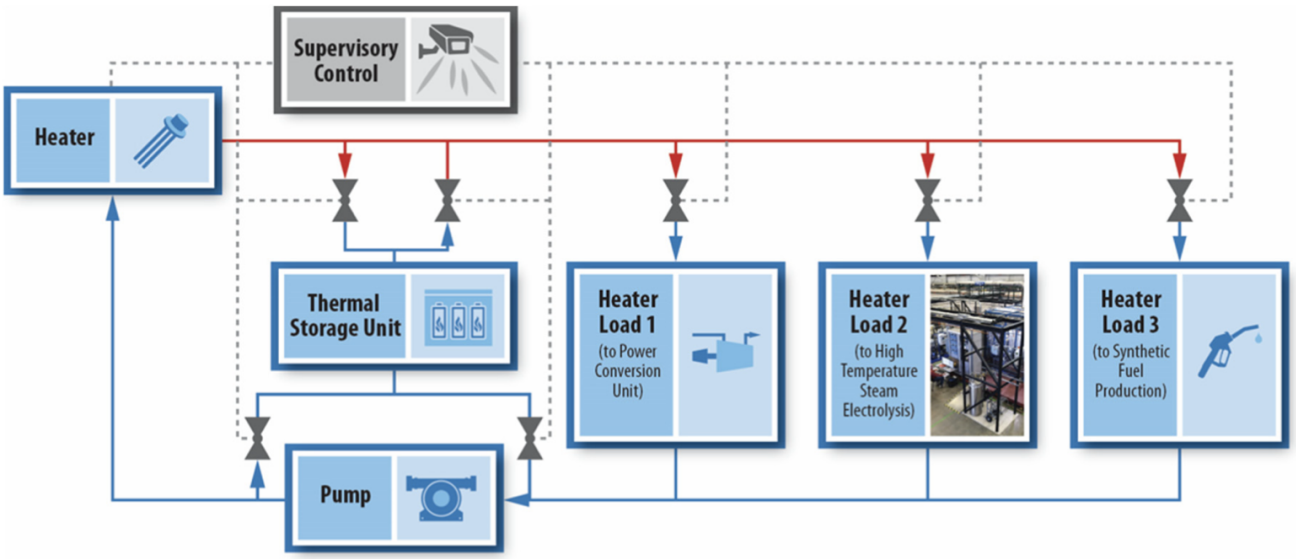

Figure 3. A TEDS schematic [16].

2.2. HTSE Overview

Although the electrolysis system mentioned in this document is referred to as the "High-Temperature Steam Electrolysis Facility", multiple electrolysis systems exist within and outside of DETAIL. Although planning and construction is ongoing, a 30 kW reversible facility is the target system to apply scaling. The stack is a solid-oxide electrolysis cell (SOEC) capable not only of running in electrolysis-cell mode to generate steady amounts of hydrogen but also designed to run in fuel-cell mode, creating electricity. Compared to the proton-exchange membrane and high-temperature thermochemical processes, SOECs are net zero carbon (if carbon dioxide is added to the cathode inlet, electrolysis of carbon dioxide is possible, making SOEC net-negative carbon) and are highly efficient due to minimal applied stack voltage. The major components are (1) the steam supply; (2) air, hydrogen, and water supplies; (3) a furnace stack; (4) an air compressor; (5) a condenser; and (6) a hydrogen recycler [17]. The hydrogen recycler process retrieves 10% of the produced hydrogen to prevent the oxidation of furnace-stack components and is initiated when the SOEC is ongoing. For proprietary purposes, schematics, design, and photos are omitted.

3. Dynamical System Scaling (DSS)

The DSS approach to system scaling is based on transforming the typical view of a process into a special, coordinate system in terms of the parameter of interest and its agents of change [18]. By parameterizing a process using a time term, which is introduced later in this section, the reproduced data can be converted into a special three-coordinate system (also called the phase space) and form a geometry with curves along the surface that contain invariant and intrinsic properties. The remainder of this section is a review of DSS theory, which was introduced into publications by Reyes [18–20] and was used in this analysis for thermocline scaling. The parameter of interest is defined as a conserved quantity within a control volume:

$$\beta(t) = \frac{1}{\Psi_0} \iiint_V \psi(\vec{x}, t) dV \tag{1}$$

where β is defined as the volume integral of the time- and space-dependent conserved quantity ψ when normalized by a time-independent value Ψ_0, which characterizes the process. The agents of change are defined as the first derivative of the normalized parameter of interest:

$$\omega = \frac{1}{\Psi_0}\frac{d}{dt}\iiint_V \psi(\vec{x},t)dV = \iiint_V \left(\phi_v + \phi_f\right)dV + \iint_A \left(\vec{j}\cdot\vec{n}\right)dA - \iint_A \psi(\vec{v}-\vec{v}_s\cdot\vec{n}dA)dA \quad (2)$$

Changes are categorized into three components: volumetric, surface, and quantity transport. The agents of change (or the frequency obtained from the units of time) are also the sum of the individual agents of change:

$$\omega = \frac{1}{\Psi_0}\frac{d}{dt}\iiint_V \psi(\vec{x},t)dV = \sum_{i=1}^{n}\omega_i$$

The relationship between ω and β is the following:

$$\omega(t) = \left.\frac{d\beta}{dt}\right|_t = \sum_{i=1}^{n}\omega_i \quad (3)$$

where ω is the first derivative of the reference time. As defined in Einstein and Infeld, time is a value that moves in constant increments [21]. The process-dependent term in DSS is called process time:

$$\tau(t) = \frac{\beta(t)}{\omega(t)} \quad (4)$$

To measure the progression difference between the reference time and process time in terms of the reference time, the idea of a temporal-displacement rate (D) is adopted:

$$D = \frac{d\tau - dt}{dt} = -\frac{\beta}{\omega^2}\frac{d\omega}{dt} \quad (5)$$

The interval of the process time is:

$$d\tau = \tau_s = (1+D)dt \quad (6)$$

Applying the process action to normalize the phase0space coordinates produces the following normalized terms:

$$\tilde{\Omega} = \omega\tau_s, \qquad \tilde{\beta} = \beta, \qquad \tilde{t} = \frac{t}{\tau_s}, \qquad \tilde{\tau} = \frac{\tau}{\tau_s}, \qquad \tilde{D} = D \quad (7)$$

The scaling relationship between the prototype and model can be defined for both β and ω and represents the scaling of the parameter of interest and its corresponding agents of change:

$$\lambda_A = \frac{\beta_M}{\beta_P}, \qquad \lambda_B = \frac{\omega_M}{\omega_P}, \qquad t_R = \frac{\lambda_A}{\lambda_B} \quad (8)$$

where the subscripts M and P stand for the model and prototype, respectively. The application of these scaling ratios to Equations (4), (5), and (10) provides the scaling ratios for other parameters as well:

$$\frac{t_M}{t_P} = \frac{\lambda_A}{\lambda_B}, \qquad \frac{\tau_M}{\tau_P} = \frac{\lambda_A}{\lambda_B}, \qquad \frac{\tilde{\beta}_M}{\tilde{\beta}_P} = \lambda_A, \qquad \frac{\tilde{\Omega}_M}{\tilde{\Omega}_P} = \lambda_A, \qquad \frac{\tilde{\tau}_M}{\tilde{\tau}_P} = 1, \qquad \frac{D_M}{D_P} = 1 \quad (9)$$

The normalized agent of change is a sum in the same respect:

$$\Omega = \sum_{i=1}^{k}\Omega_i \quad (10)$$

The ratio of Ω is expressed in the following alternative form:

$$\Omega_R = \frac{\Omega_M}{\Omega_P} = \frac{\sum_{i=1}^{k} \Omega_{M,i}}{\sum_{i=1}^{k} \Omega_{P,i}} = \frac{\Omega_{M,1} + \Omega_{M,2} + \ldots + \Omega_{M,k}}{\Omega_{P,1} + \Omega_{P,2} + \ldots + \Omega_{P,k}} \tag{11}$$

By the law of scaling ratios, the following must be true:

$$\lambda_A = \frac{\Omega_{M,1}}{\Omega_{P,1}}, \lambda_A = \frac{\Omega_{M,2}}{\Omega_{P,2}}, \ldots, \lambda_A = \frac{\Omega_{M,k}}{\Omega_{P,k}} \tag{12}$$

4. Connective Components—Shell-and-Tube Heat Exchanger and Helical Steam-Generator System Equation Scaling

Two types of heat exchangers are used in TEDS. The first one is assumed to be a shell-and-tube heat exchanger for TTSS thermal charging. (Currently, heat is injected via a power rod, and an actual heat exchanger will be installed in the future.) The second is a helical steam generator for TTSS thermal discharge and steam supply for the HTSE system. The following equations will address the mechanical and thermal characteristics of heat exchangers in general.

4.1. Overall Heat Transfer Equation

The overall heat transfer is justified by considering the heat-exchanger volume as one system. Typically, the total heat transfer can be assessed using the temperature difference:

$$Q = U \times A_{overall} \times LMTD \tag{13}$$

where U, $A_{overall}$, and $LMTD$ are the overall heat transfer coefficient, overall heat transfer surface area, and logarithmic-mean temperature difference ($LMTD$).

For heat exchangers, the overall heat-transfer coefficient can be determined using local heat-transfer coefficients and their relation in parallel. Because the flow in heat exchangers is either parallel or counter flow, the shell and tubes are oriented such that heat transfer occurs among the shell, outer tube, and inner tube (when assuming axisymmetry):

$$\frac{1}{U} = \left[\frac{1}{h_0} + R_{do} + \frac{A_o}{A_i}\left(\frac{OD - ID}{2k_w}\right) + \frac{A_o}{A_i}\left(\frac{1}{h_i}\right) + \frac{A_o}{A_i}R_i\right] \tag{14}$$

where h_o, h_i, R_{do}, R_{di}, A_o, A_i, k_w, ID, and OD are the shell-side heat-transfer coefficient, tube-side heat-transfer coefficient, shell-side dirt factor, tube-side dirt factor, outer surface area of the tube, inner surface area of the tube, conductive heat-transfer coefficient of the tube wall, tube inner diameter, and tube outer diameter.

The temperature difference is represented by the logarithmic-mean temperature difference and is an average quantification of the temperature difference between the shell and tube sides:

$$LMTD = \frac{\Delta T_1 - \Delta T_2}{\ln\left(\frac{\Delta T_1}{\Delta T_2}\right)} \tag{15}$$

where ΔT_1 and ΔT_2 are the temperature difference of the hot and cold fluids at one end of the heat exchanger and the temperature difference of the hot and cold fluids at the other end of the heat exchanger.

However, the $LMTD$ is valid only for heat exchangers with one shell pass and one tube pass. For multiple shell and tube passes, the flow pattern in a heat exchanger is neither purely co-current nor purely counter-current. Thus, to account for the geometric irregularity, $LMTD$ must be multiplied by a mean temperature difference (MTD) correction factor (F_T) to obtain the corrected MTD. The corrected MTD is:

$$LMTD = \frac{\Delta T_1 - \Delta T_2}{\ln\left(\frac{\Delta T_1}{\Delta T_2}\right)} \times F_T \tag{16}$$

4.2. Simplified Fluid Mechanics

Due to the various geometries of heat exchangers, mass and momentum equations can differ. To generalize the fluid momentum based on the number of tubes and passes, the tube velocity can be expressed as the following:

$$v_T = \frac{4\dot{m}}{\pi\rho ID^2}\frac{N_P}{N_T} \tag{17}$$

where $\dot{m}$, N_P, N_T, and ρ represent the mass-flow rate on the tube side, the number of tube passes, the number of tubes, the tube-side fluid density, and the tube internal diameter.

The number of required tubes can be approximated by considering the required total heat-transfer area:

$$N_T = \frac{A_{overall}}{\pi OD \times L} \tag{18}$$

where L is the total tube length. Using Equation (17), the tube's Reynolds number is:

$$Re = \frac{4\dot{m}}{\pi\mu ID}\frac{N_P}{N_T} \tag{19}$$

where μ is the dynamic viscosity.

5. Connective Components—Pipe-System Equation Scaling

The mass, momentum, and energy-conservation equations are the governing physics for pipe systems and are well documented. Assuming axisymmetry and a fully developed flow, the simplified mass, momentum, and energy-conservation equations are Equations (20)–(22):

$$\frac{\partial\rho}{\partial t} = -v_z\frac{\partial\rho}{\partial z} - \rho\frac{\partial v_z}{\partial z} \tag{20}$$

$$\frac{\partial v_z}{\partial t} = -\frac{v_z}{\rho}\frac{\partial\rho}{\partial t} - \frac{1}{\rho}\frac{\partial P}{\partial z} + \nu\left(\frac{1}{r}\frac{\partial v_z}{\partial r} + \frac{\partial^2 v_z}{\partial r^2}\right) \tag{21}$$

$$\frac{\partial T}{\partial t} = \frac{\alpha}{r}\frac{\partial T}{\partial r} + \frac{\partial\alpha}{\partial r}\frac{\partial T}{\partial r} + \alpha\frac{\partial^2 T}{\partial r^2} + \frac{\partial\alpha}{\partial z} + \alpha\frac{\partial^2 T}{\partial z^2} + \frac{\mu}{\rho c_P}\frac{\partial v_z}{\partial r} - v_z\frac{\partial T}{\partial z} \tag{22}$$

6. Thermal Energy Distribution System—Thermocline Thermal Storage System Equation Scaling

The TTSS sits between the hot and cold lines that allow flows from either section, depending on the operation mode [16,22]. The following sections both characterize the conservation rules and non-dimensionalize the process when necessary.

6.1. Mass-Flow Rate

When the mass flow rate from the inlet is m, then by conservation of mass, the mass-flow rate within the TTSS must be the equivalent:

$$\dot{m} = \rho_{in}v_{z,in}\pi R_{in}^2 = \rho_{th}v_{z,th}\varepsilon\pi R_{th}^2 \tag{23}$$

where ρ_{in} is the inlet density, ρ_{th} is the TTSS density, $v_{z,in}$ is the inlet axial velocity, $v_{z,th}$ is the TTSS axial velocity, R_{in} is the inlet pipe radius, ε is the porosity (ratio of fluid to filler), and R_{th} is the TTSS fluid-tank radius. The TTSS axial velocity is the following:

$$v_{z,th} = \frac{\rho_{in}R_{in}^2 v_{z,in}}{\rho_{th}\varepsilon R_{th}^2} \tag{24}$$

6.2. Conservation of Mass

In cylindrical coordinates, the compressible conservation of mass is:

$$\frac{\partial \rho_{th}}{\partial t} + \frac{1}{r}\frac{\partial(\rho_{th} r v_{r,th})}{\partial r} + \frac{v_{\theta,th}}{r}\frac{\partial(\rho_{th} v_{\theta,th})}{\partial \theta} + \frac{\partial v_{z,th}}{\partial z} = 0 \tag{25}$$

where $v_{r,th}$ is the TTSS radial velocity, and $v_{\theta,th}$ is the TTSS azimuthal velocity. By expanding the terms and ignoring the radial and azimuthal velocities, the differential density is:

$$\frac{\partial \rho_{th}}{\partial t} = -v_z \frac{\partial \rho_{th}}{\partial z} - \rho_{th}\frac{\partial v_z}{\partial z} \tag{26}$$

6.3. Conservation of Momentum

In cylindrical coordinates, the compressible conservation of momentum in the axial direction is:

$$\frac{D(\rho_{th} v_{z,th})}{Dt} = -\frac{\partial P}{\partial z} + \mu_{th}\left(\frac{1}{r}\frac{\partial}{\partial r}\left[r\frac{\partial v_{z,th}}{\partial r}\right] + \frac{1}{r^2}\frac{\partial^2 v_{z,th}}{\partial \theta^2} + \frac{\partial^2 v_{z,th}}{\partial z^2}\right) \tag{27}$$

where P is the TTSS internal pressure. By expanding the terms, the differential axial velocity is:

$$\frac{\partial v_{z,th}}{\partial t} = -\frac{v_{z,th}}{\rho_{th}}\frac{\partial \rho_{th}}{\partial t} - \frac{1}{\rho_{th}}\frac{\partial P}{\partial z} + \nu\left(\frac{1}{r}\frac{\partial v_{z,th}}{\partial r} + \frac{\partial^2 v_{z,th}}{\partial r^2} + \frac{\partial^2 v_{z,th}}{\partial z^2}\right) \tag{28}$$

6.4. Conservation of Energy

From Konor et al. [16], the thermocline heat-transfer equation that characterizes the energy conservation of a fluid flow through porous media for low- and no-flows is (originally from Gunn (1978) [23] and modified in [24]):

$$\rho_{th} c_{P,th} \varepsilon \pi R_{th}^2 dz \frac{\partial T_{th}}{\partial t} = \rho_{th} \varepsilon \pi R_{th}^2 v_{z,th}(h_z - h_{z+dz}) + h_c S_r\left(T_{fr} - T_{th}\right)dz + \dot{Q}_{losses} \tag{29}$$

where ε is the porosity, h_z is the specific enthalpy of the current node, h_{z+dz} is the specific enthalpy of the next axial node, h_c is the convective heat-transfer coefficient between the fluid and filler, S_{fr} is the heat-transfer area of filler per unit length of the tank, T_{fr} is the filler temperature, T_{th} is the TTSS fluid temperature, dz is the axial distance between each node, and $\dot{Q}_{losses}$ is the heat conduction through the walls. When specific enthalpy is replaced by specific heat and temperature at the node, the heat-transfer equation is:

$$\begin{aligned}\rho_{th} c_{P,th} \varepsilon \pi R_{th}^2 dz \frac{\partial T_{th}}{\partial t} &= \rho_{th} \varepsilon \pi R_{th}^2 v_{z,th}(c_{P,z,th} T_{th,z} - c_{P,z+dz,th} T_{th,z+dz}) \\ &\quad + h_c S_r\left(T_{fr} - T_{th}\right)dz + \dot{Q}_{losses}\end{aligned} \tag{30}$$

By dividing both sides by dz and considering the specific-enthalpy difference portion as a form of first-order forward numeric differentiation, the difference can be rewritten as the spatial first derivative of the specific enthalpy in the axial direction:

$$\rho_{th} c_{P,th} \varepsilon \pi R_{th}^2 \frac{\partial T_{th}}{\partial t} = \rho_{th} \varepsilon \pi R_{th}^2 v_{z,th}\frac{\partial (c_{P,th} T_{th})}{\partial z} + h_c S_r\left(T_{fr} - T_{th}\right) + \frac{\dot{Q}_{losses}}{dz} \tag{31}$$

By using Equation (19) for the TTSS axial velocity and expanding the terms, it can be reorganized as:

$$\frac{\partial T_{th}}{\partial t} = \frac{\rho_{in} R_{in}^2 v_{z,in}}{\rho_{th} c_{P,th} R_{th}^2}\left(T_{th}\frac{\partial c_{P,th}}{\partial z} + c_{P,th}\frac{\partial T_{th}}{\partial z}\right) + \frac{h_c S_r\left(T_{fr} - T_{th}\right)}{\rho_{th} c_{P,th} \varepsilon \pi R_{th}^2} + \frac{\dot{Q}_{losses}}{\rho_{th} c_{P,th} \varepsilon \pi R_{th}^2 dz} \tag{32}$$

The wall losses can be expressed by representing the heat transfer radially across the wall to the outer ambient air:

$$\frac{\partial T_{th}}{\partial t} = \frac{\rho_{in} R_{in}^2 v_{z,in}}{\rho_{th} c_{P,th} R_{th}^2}\left(T_{th}\frac{\partial c_{P,th}}{\partial z} + c_{P,th}\frac{\partial T_{th}}{\partial z}\right) + \frac{h_c S_r\left(T_{fr} - T_{th}\right)}{\rho_{th} c_{P,th} \varepsilon \pi R_{th}^2} + \frac{\pi R_w^2}{\rho_{th} c_{P,th} \varepsilon \pi R_{th}^2}\left(\frac{k}{r}\frac{\partial T_w}{\partial r} + \frac{\partial k}{\partial r}\frac{\partial T_w}{\partial r} + k\frac{\partial^2 T_w}{\partial r^2}\right) \quad (33)$$

where T_w is the wall temperature.

7. High-Temperature Steam Electrolysis—Solid-Oxide Electrolysis Cell Stack-System Equation Scaling

The HTSE system is composed of two major subsystems to generate hydrogen at the specified rate: the preheater and SOEC stack. These subsystems include inputs from the trim and stack heaters, steam supply from the heat exchanger, and other parameters that represent conditions for hydrogen production. As the following sections introduce preheater thermal dynamics, stack electrical dynamics, and stack thermal dynamics, the electrode feed factors, gas-outlet partial pressure, average gas partial pressure, and gas-outlet flow rate expressions will be provided first. The following relations and equations are from [25,26].

7.1. Electrode Feed Factors

The feed factors are the ratio of gas-steam and electrolyzer feedbacks. For the cathode-side chamber, high-temperature steam (H_2O) is provided and is electrolyzed.

$$\pi_{ca} = \frac{H_2O \text{ provided in cathode stream}}{H_2O \text{ consumed by electrolysis}} = \frac{w_{H_2O,in}}{\frac{n_c I}{2F}} \quad (34)$$

where π_{ca}, $w_{H_2O,in}$, I, and F are the cathode feed factor, steam-inlet molar flow rate, stack current, and Faraday's constant. For the anode-side chamber, air and oxygen ions are supplied.

$$\pi_{an} = \frac{O_2 \text{ provided in anode stream}}{O_2 \text{ generated by electrolysis}} = \frac{w_{O_2,in}}{\frac{n_c I}{4F}} \quad (35)$$

where π_{an} and w_{O_2} are the anode feed factor and oxygen inlet molar flow rate. The 2 value in the denominator of Equations (34) and (35) reflects the cathode reduction and anode oxidization shown in Equation (36).

$$\begin{aligned} &\text{Cathode Reduction: } 2H_2O + 4e^- \rightarrow 2H_2 + 2O^{2-} \\ &\text{Anode Oxidization: } 2O^{2-} \rightarrow O_2 + 4e^- \end{aligned} \quad (36)$$

Essentially, for every hydrogen molecule (H_2) generated, half of a water molecule and one-half of an oxygen molecule (O_2) are required.

7.2. Gas-Outlet Partial Pressure

Using the mass balance and assuming no mass diffusion at the stack inlet or outlet, the outlet pressures can be expressed in terms of feed factors and inlet pressures.

$$\begin{aligned} P_{H_2O,out} &= \frac{(\pi_{ca} - 1)}{\pi_{ca}} P_{H_2O,in} \\ P_{H_2,out} &= P_{H_2,in}\frac{1}{\pi_{ca}} P_{H_2,in} \\ P_{O_2,out} &= \frac{(\pi_{an} + 1)}{\pi_{an+P_{O_2,in}}} PO_2, in \\ P_{N_2,out} &= \frac{\pi_{an} P_{N_2,in}}{\pi_{an} + P_{N_2,in}} \end{aligned} \quad (37)$$

where $P_{H_2O,out}$ is the outlet steam pressure, $P_{H_2O,in}$ is the inlet steam pressure, $P_{H_2,out}$ the outlet hydrogen pressure, $P_{H_2,in}$ the inlet hydrogen pressure, $P_{O_2,out}$ the outlet oxygen pressure, $P_{O_2,in}$ the inlet oxygen pressure, $P_{N_2,out}$ the outlet nitrogen pressure, and $P_{N_2,in}$ the inlet nitrogen pressure.

7.3. Average Gas Partial Pressure

Assuming lumped pressures are valid for steady state when both current and feed flows are included in the feed factors, the required average gas-pressure cell voltage evaluation is:

$$\begin{aligned}
\bar{P}_{H_2O} &= P_{H_2O,in}^{(1-\lambda)} P_{H_2O,out}^{\lambda} \times \frac{1}{1+s\tau_{H_2O}} \\
\bar{P}_{H_2} &= P_{H_2,in}^{(1-\lambda)} P_{H_2,out}^{\lambda} \times \frac{1}{1+s\tau_{H_2}} \\
\bar{P}_{O_2} &= P_{O_2,in}^{(1-\lambda)} P_{O_2,out}^{\lambda} \times \frac{1}{1+s\tau_{O_2}} \\
\bar{P}_{N_2} &= P_{N_2,in}^{(1-\lambda)} P_{N_2,out}^{\lambda} \times \frac{1}{1+s\tau_{N_2}}
\end{aligned} \tag{38}$$

where λ is a constant selected through a parametric study for lumped pressures, s is the Laplace variable, $\bar{P}_{H_2O}$ is the average steam pressure, τ_{H_2O} is the steam first-order delay constant, $\bar{P}_{H_2}$ is the average hydrogen pressure, τ_{H_2} is the hydrogen first-order delay constant, $\bar{P}_{O_2}$ is the average oxygen pressure, tau_{O_2} is the oxygen first-order delay constant, $\bar{P}_{N_2}$ is the average nitrogen pressure, and τ_{N_2} is the nitrogen first-order delay constant.

7.4. Outlet Flow Rates

Considering the inlet flow rate introduced in Equation (34), the outlet flow rates of different reactants are the following:

$$\begin{aligned}
w_{H_2O,out} &= w_{H_2O,in} - \frac{n_c I}{2F} \\
w_{H_2,out} &= w_{H_2,in} + \frac{n_c I}{F} \\
w_{O_2,out} &= w_{O_2,in} + \frac{n_c I}{4F} \\
w_{N_2,out} &= w_{N_2,in}
\end{aligned} \tag{39}$$

where $w_{H_2O,out}$, $w_{H_2,out}$, $w_{O_2,out}$, and $w_{N_2,out}$ are the steam outlet molar flow rate, hydrogen outlet molar flow rate, oxygen outlet molar flow rate, and nitrogen outlet molar flow rate, respectively. The plus and minus signs in Equation (39) indicate how the electrolysis process affects incoming-gas flow rates. For nitrogen, because there is no consumption or generation, the flow rate remains constant.

7.5. Stack Electrical Dynamics

Stack electrodynamics cover the dynamic behavior of applied stack voltage considering that the Nernst voltage is due to differences in hydrogen and oxygen partial pressure on the two sides of a single cell [27], the electrical resistances of the cell structure, and the required voltage to match the electrode's activation energy (reactant starvation is neglected). The combined dynamic behavior to the stack voltage is called the overvoltage and is the following:

$$V(I,\bar{T},\bar{P}) = V_{rev}(\bar{T},\bar{P}) + V_{ohm}(I,\bar{T}) + V_{act}(I,\bar{T}) \cdot \frac{1}{1+s\tau_{act}} \tag{40}$$

where V is the stack voltage, $\bar{T}$ is the average temperature, V_{rev} is the reversible overvoltage, V_{ohm} is the ohmic overvoltage, V_{act} is the activation overvoltage, and τ_{act} is the activation first-order delay constant.

7.5.1. Reversible Overvoltage

The cell reversible effects due to hydrogen and oxygen partial pressures can be expressed using the Nernst equation:

$$V_{rev}(\bar{T}, \bar{P}) = V_{oc}(\bar{T}) + \frac{R\bar{T}}{2F} \ln\left(\frac{\bar{P}_{H_2}\bar{P}_{O_2}^{0.5}}{\bar{P}_{H_2O}}\right) \tag{41}$$

where V_{oc} and R are the open circuit voltage and gas constant, respectively. The open-circuit voltage is associated with the reaction's Gibbs free energy:

$$V_{oc}(\bar{T}) = \frac{\Delta G(\bar{T})}{2F} \tag{42}$$

The reference Gibbs free energy is approximated to be (in a modification of [28]):

$$\Delta G(\bar{T}) = 244,800 - 49.18 \cdot \bar{T} - 2.72 \cdot 10^{-3} \cdot \bar{T}^2 \tag{43}$$

7.5.2. Ohmic Overvoltage

The electrical resistances of cell-structure effects can be expressed using Ohm's law:

$$V_{ohm}(I, \bar{T}) = I \cdot A^{-1} \cdot ASR(\bar{T}) \tag{44}$$

where A and ASR are the cell area and area-specific resistance of the cell, respectively. The area-specific resistance for SOEC cells is [29]:

$$ASR(\bar{T}) = ASR\left(T_{ref}\right) - 0.463 + 3.973 \cdot e^{\frac{10,300}{\bar{T}}} \tag{45}$$

7.5.3. Activation Overvoltage

The required voltage to match electrode activation energy is approximated using the Butler–Volmer equation:

$$V_{act}(I, \bar{T}) = \frac{R\bar{T}}{2F}\left[\sinh^{-1}\left(\frac{i}{2I_{ex,ca}}\right) + \sinh^{-1}\left(\frac{i}{2I_{ex,an}}\right)\right] \tag{46}$$

where i is the stack current density, and $I_{ex,ca}$ and $I_{ex,an}$ are the cathode and anode exchange currents, respectively. Using the pre-exponential factor (Γ_{ex}) and activation energy (ξ), the exchange current is:

$$I_{ex,ca} = \frac{R\bar{T}}{2F}\Gamma_{ex,ca}e^{-\frac{\xi_{ca}}{R\bar{T}}}, I_{ex,an} = \frac{R\bar{T}}{2F}\Gamma_{ex,an}e^{-\frac{\xi_{an}}{R\bar{T}}} \tag{47}$$

where $\Gamma_{ex,ca}$ is the cathode pre-exponential factor, $\Gamma_{ex,an}$ the anode pre-exponential factor, ξ_{ca} the cathode activation energy, and ξ_{an} the anode activation energy.

7.6. Stack Thermal Dynamics

When considering the energy balance of the SOEC stack as the control volume, the stored heat is an equation about the supplied power, the power required to sustain the steam-electrolysis process, the power required to warm steam, and the power needed to maintain stack temperature:

$$C_{P,\text{SOEC}}\frac{\partial \bar{T}}{\partial t} = n_c V I - P_{rea}(T_{out}) - P_{war}(T_{in}, T_{out}, w_{in}) + P_{heat} \tag{48}$$

where $C_{P,\mathrm{SOEC}}$ is the equivalent SOEC heat capacity, P_{rea} is the electrolysis-reaction power, P_{war} is the steam-warming power, and P_{heat} is the stack heater power. Using the strong correlation with stack average temperature, the stack outlet temperature can be approximated to be proportional to the stack average temperature [25]:

$$T_{out} = k\bar{T} \tag{49}$$

where T_{out} and k are the stack outlet temperature and multiplication factor, respectively. The multiplication factor is estimated by measurements. Sections 7.6.1 and 7.6.2 denote the components of stack thermal dynamics.

7.6.1. Electrolysis Reaction Power

Electrolysis reaction power is associated with the enthalpy of the change caused by the electrolysis process. Once the enthalpy change is known, Faraday's constant allows the representation of the thermal contribution to electrical potential:

$$P_{rea}(T_{out}) = n_c I V_{th} = n_c \cdot \frac{\Delta H_R(T_{out})}{2F} \approx n_c I \cdot \frac{\Delta H_R(k_T \bar{T})}{2F} \tag{50}$$

The enthalpy change by correlation, using the existing experimental data, is:

$$\Delta H_R(T_{out}) = 238,200 - 13.12 \cdot T_{out} - 3.55 \cdot 10^{-3} \cdot T_{out}^2 \tag{51}$$

7.6.2. Steam-Warming Power

The warming power is associated with the enthalpy increase and can be expressed using the specific heat of each species existing in the stack and the corresponding temperature change, assuming that each specie shares the same temperature. The weight of each specie can be characterized by using the corresponding gas-inlet flow rate:

$$P_{war}(T_{in}, T_{out}, w_{in}) = (T_{out} - T_{in})\left(c_{P,H_2O} \cdot w_{H_2O} + c_{P,H_2} \cdot w_{H_2} + c_{P,O_2} \cdot w_{O_2} + c_{P,N_2} \cdot w_{N_2}\right) \tag{52}$$

where c_{P,H_2O} is the steam specific heat, c_{P,H_2} is the hydrogen specific heat, c_{P,O_2} is the oxygen specific heat, and c_{P,N_2} is the nitrogen specific heat.

7.7. Preheater Thermal Dynamics

Similar to stack thermal dynamics, the energy balance of the preheater with the power required to warm steam and to supply the heater:

$$C_{P,pre}\frac{\partial T_{in}}{\partial t} = P_{heat,pre} - P_{war,pre}(1-\epsilon)(T_{in}, T_{steam}, T_{amb}, w_{in}) \tag{53}$$

where $C_{P,pre}$ and $P_{war,pre}$, and ϵ are the preheater heat capacity, preheater steam-warming power, and heat-recycle ratio, respectively. The heat -recycle ratio takes into account the effectiveness of fuel heat exchangers recycling heat from the SOEC-outlet steam. Section 7.7.1 shows the preheater steam-warming power components.

7.7.1. Preheater Steam-Warming Power

The preheater warming power is the enthalpy increase contribution from the existing species in the preheater. For steam and hydrogen, the temperature difference between the preheater outlet temperature (or so called, inlet SOEC temperature) and initial steam temperature is used to calculate the amount of heat removal. For oxygen and nitrogen, the temperature difference between the preheater outlet temperature and ambient temperature is used. As shown in Section 7.6.2, the weights of each specie can be characterized by using the corresponding gas-inlet flow rate:

$$\begin{aligned} P_{war}(T_{in}, T_{steam}, T_{amb}, w_{in}) = {} & (T_{in} - T_{steam})\left(c_{P,H_2O} \cdot w_{H_2O} + c_{P,H_2} \cdot w_{H_2}\right) \\ & + (T_{in} - T_{amb})\left(c_{P,O_2} \cdot w_{O_2} + c_{P,N_2} \cdot w_{N_2}\right) \end{aligned} \tag{54}$$

where T_{steam} and T_{amb} are the initial steam temperature and ambient temperature, respectively.

8. Scaled Equations

In order to determine the scaled ratios based on the test case in Section 10, the scaled equations of each system are required. Sections 8.1–8.4 show either the scaling process or the finished products.

8.1. Heat Exchangers

As shown in Section 4, the equations provided for shell-and-tube heat exchangers and helical steam generators are common and are essentially vessels to transport thermal energy from one independent system to another. Each identified equation is non-dimensionalized to address the scaled form. Starting from Equation (13), the parameter of interest is the overall heat transfer, where the dimensionless form is $Q^+ = Q/Q_0$, and Q_0 is the nominal heat transfer. It can be reorganized as the following:

$$\frac{Q^+}{U} = \frac{A_{overall} \times LMTD}{Q_0} \tag{55}$$

Using the known variables from Equations (14), (17), and (18), the intermediate non-dimensionalized form of Equation (55) is:

$$Q^+\left[\frac{1}{h_0} + \frac{A_o}{A_i}\left(\frac{OD - ID}{2k_w}\right) + \frac{A_o}{A_i}\left(\frac{1}{h_i}\right)\right] = \frac{4\dot{m}LN_P \times OD}{\rho v_T Q_0 \times ID^2} LMTD \tag{56}$$

Because tube velocity is essential for determining flow conditions and heat transfer, it will be non-dimensionalized by $v_T^+ = v_T/v_{T,0}$, where $v_{T,0}$ is the nominal velocity. In order to characterize the temperature difference experienced in the heat exchanger, the components of the LMTD (shown in Equation (15)) are also expanded:

$$Q^+\left[\frac{1}{h_0} + \frac{A_o}{A_i}\left(\frac{OD - ID}{2k_w}\right) + \frac{A_o}{A_i}\left(\frac{1}{h_i}\right)\right] = \frac{4\dot{m}LN_P \times OD}{\rho v_{T,0} v_T^+ Q_0 \times ID^2} \frac{(T_{shell,in} - T_{tube,in}) - (T_{shell,out} - T_{tube,out})}{\ln\left(\frac{T_{shell,in} - T_{tube,in}}{T_{shell,out} - T_{tube,out}}\right)} F_T \tag{57}$$

where $T_{shell,in}$ represents the shell-inlet temperature, $T_{tube,in}$ the tube-inlet temperature, $T_{shell,out}$ the shell-outlet temperature, and $T_{tube,out}$ the tube-outlet temperature. Depending on the location of the temperature measurements, temperature scaling is helpful in determining the thermal relations to other systems. Temperature is non-dimensionalized using $T^+ = T/T_0$, where T_0 is the nominal temperature for the given location:

$$\begin{aligned} Q^+\left[\frac{1}{h_0} + \frac{A_o}{A_i}\left(\frac{OD - ID}{2k_w}\right) + \frac{A_o}{A_i}\left(\frac{1}{h_i}\right)\right] &= \frac{4\dot{m}LN_P F_T \times OD}{\rho v_{T,0} v_T^+ Q_0 \times ID^2} \\ \frac{T_{shell,in,0} T_{shell,in}^+ - T_{tube,in,0} T_{tube,in}^+ - T_{shell,out,0} T_{shell,out}^+ + T_{tube,out,0} T_{tube,out}^+}{\ln\left(\frac{T_{shell,in} - T_{tube,in}}{T_{shell,out} - T_{tube,out}}\right)} & \end{aligned} \tag{58}$$

The scaled ratios are determined by using the form:

$$\text{ratio} = \frac{\text{target system}}{\text{prototype system}} \tag{59}$$

By applying Equation (59) to Equation (58)'s left- and right-hand sides, the scaled form is derived expressing the overall heat transfer, tube velocity, and shell-inlet, tube-inlet, shell-outlet, and tube-outlet temperature as $\lambda_{A,Q} = Q_{target}^+/Q_{prototype}^+$, $\lambda_{A,v_T} = v_{T,target}^+/v_{T,prototype}^+$, $\lambda_{A,T_{shell,in}} = T_{shell,in,target}^+/T_{shell,in,prototype}^+$, $\lambda_{A,T_{tube,in}} = T_{tube,in,target}^+/T_{tube,in,prototype}^+$, $\lambda_{A,T_{shell,out}} = T_{shell,out,target}^+/T_{shell,out,prototype}^+$, and $\lambda_{A,T_{tube,out}} = T_{tube,out,target}^+/T_{tube,out,prototype}^+$.

$$\lambda_{A,Q}\left[\frac{1}{h_0}+\frac{A_o}{A_i}\left(\frac{OD-ID}{2k_w}\right)+\frac{A_o}{A_i}\left(\frac{1}{h_i}\right)\right]_R=\left[\frac{\dot{m}LN_PF_T\times OD}{\rho v_{T,0}Q_0\times ID^2}\right]_R\frac{1}{\lambda_{A,v_T}}$$
$$\left[\frac{T_{shell,in,0}T^+_{shell,in}-T_{tube,in,0}T^+_{tube,in}-T_{shell,out,0}T^+_{shell,out}+T_{tube,out,0}T^+_{tube,out}}{\ln\left(\frac{T_{shell,in}-T_{tube,in}}{T_{shell,out}-T_{tube,out}}\right)}\right]_R \quad (60)$$

As is shown in Equation (12), the law of scaled ratios allows numerators and denominators of the same component to be separated when strictly enforcing a certain value. Applying the law of scaling ratio to Equation (60) yields the following relations:

$$\begin{aligned}\left[\frac{1}{h_o}\right]_R\lambda_{A,Q}&=\left[\frac{A_o}{A_i}\left(\frac{OD-ID}{k_w}\right)\right]_R\lambda_{A,Q}=\left[\frac{A_o}{A_i}\left(\frac{1}{h_i}\right)\right]_R\lambda_{A,Q}\\&=\left[\frac{\dot{m}LN_PF_T\times OD}{\rho v_{T,0}Q_0\times ID^2}\right]_R\left[\frac{1}{\ln\left(\frac{T_{shell,in}-T_{tube,in}}{T_{shell,out}-T_{tube,out}}\right)}\right]_R[T_{shell,in,0}]_R\frac{\lambda_{A,T_{shell,in}}}{\lambda_{A,v_T}}\\&=\left[\frac{\dot{m}LN_PF_T\times OD}{\rho v_{T,0}Q_0\times ID^2}\right]_R\left[\frac{1}{\ln\left(\frac{T_{shell,in}-T_{tube,in}}{T_{shell,out}-T_{tube,out}}\right)}\right]_R[T_{tube,in,0}]_R\frac{\lambda_{A,T_{tube,in}}}{\lambda_{A,v_T}}\\&=\left[\frac{\dot{m}LN_PF_T\times OD}{\rho v_{T,0}Q_0\times ID^2}\right]_R\left[\frac{1}{\ln\left(\frac{T_{shell,in}-T_{tube,in}}{T_{shell,out}-T_{tube,out}}\right)}\right]_R[T_{shell,out,0}]_R\frac{\lambda_{A,T_{shell,out}}}{\lambda_{A,v_T}}\\&=\left[\frac{\dot{m}LN_PF_T\times OD}{\rho v_{T,0}Q_0\times ID^2}\right]_R\left[\frac{1}{\ln\left(\frac{T_{shell,in}-T_{tube,in}}{T_{shell,out}-T_{tube,out}}\right)}\right]_R[T_{tube,out,0}]_R\frac{\lambda_{A,T_{tube,out}}}{\lambda_{A,v_T}}\end{aligned} \quad (61)$$

where the ratio of the LMTD denominator and correction factor can be assessed by considering the systems being scaled.

8.2. Pipe System

From Section 5, the equations for mass, momentum, and energy conservation are provided. Following the same process as Section 8.1, each equation is non-dimensionalized to address the scaled form. Sections 8.2.1–8.2.3 show the steps to achieve the scaled forms.

8.2.1. Mass

Starting from Equation (20), the parameters of interest are fluid density; fluid velocity, where the corresponding dimensionless form is $\rho^+=\rho/\rho_0$; and v_z^+, where ρ_0 and $v_{z,0}$ are the nominal fluid density and nominal axial velocity, respectively:

$$\frac{\partial\rho^+}{\partial t}=-v_{z,0}v_z^+\frac{\partial\rho^+}{\partial z}-v_{z,0}\rho^+\frac{\partial v_z^+}{\partial z} \quad (62)$$

By applying Equation (59) to Equation (62)'s left- and right-hand sides, the scaled form is derived to express the fluid density, fluid-density agents of change, and fluid velocity as $\lambda_{A,\rho}=\frac{\rho^+_{target}}{\rho^+_{prototype}}$, $\lambda_{B,\rho}=\frac{\frac{\partial\rho^+}{\partial t}_{target}}{\frac{\partial\rho^+}{\partial t}_{prototype}}$, and $\lambda_{A,v_z}=\frac{v^+_{z,target}}{v^+_{z,prototype}}$.

$$\lambda_{B,\rho}=\left[-v_{z,0}v_z^+\frac{\partial\rho^+}{\partial z}-v_{z,0}\rho^+\frac{\partial v_z^+}{\partial z}\right]_R \quad (63)$$

Following Equation (12) and the law of scaled ratios, the following is the derived relation:

$$\lambda_{B,\rho}=\left[\frac{v_{z,0}}{\Delta z}\right]_R\lambda_{A,v_z}\lambda_{A,\rho} \quad (64)$$

From Equation (8), the time ratio is $t_R=\lambda_A/\lambda_B$. Applying this to Equation (63), the time ratio can be newly defined as the following:

$$t_R = \frac{\Delta z_R}{\lambda_{A,v_z}} \tag{65}$$

8.2.2. Momentum

Starting from Equation (21), the parameters of interest are fluid density and velocity. Again:

$$\frac{\partial v_z^+}{\partial t} = -\frac{v_z^+}{\rho^+}\frac{\partial \rho^+}{\partial t} - \frac{1}{v_{z,0}\rho_0}\frac{1}{\rho^+}\frac{\partial P}{\partial z} + \nu\left(\frac{1}{r}\frac{\partial v_z^+}{\partial r} + \frac{\partial^2 v_z^+}{\partial r^2}\right) \tag{66}$$

By applying Equation (59) to Equation (66)'s left- and right-hand sides, the scaled form is derived expressing the fluid density, fluid-density agents of change, fluid velocity from Equation (62), and fluid-velocity agents of change as $\lambda_{B,v_z} = \frac{\frac{\partial v_z^+}{\partial t}_{target}}{\frac{\partial v_z^+}{\partial t}_{prototype}}$.

$$\lambda_{B,v_z} = \left[-\frac{v_z^+}{\rho^+}\frac{\partial \rho^+}{\partial t} - \frac{1}{v_{z,0}\rho_0}\frac{1}{\rho^+}\frac{\partial P}{\partial z} + \nu\left(\frac{1}{r}\frac{\partial v_z^+}{\partial r} + \frac{\partial^2 v_z^+}{\partial r^2}\right)\right]_R \tag{67}$$

Following Equation (12) and the law of scaled ratios, the following is the derived relation:

$$\lambda_{B,v_z} = \frac{\lambda_{A,v_z}\lambda_{B,\rho}}{\lambda_{A,\rho}} = \left[\frac{P}{\Delta z}\right]_R \frac{1}{\lambda_{A,\rho}} = \left[\frac{\nu}{r^2}\right]_R \lambda_{A,v_z} \tag{68}$$

Applying the time-ratio concept, the second term in Equation (68) is:

$$\frac{\lambda_{A,v_z}\lambda_{B,\rho}}{\lambda_{A,\rho}} \rightarrow \frac{\lambda_{A,v_z}}{t_R} \tag{69}$$

Thus, a new form of the time ratio can be defined as the following:

$$t_R = \left[\frac{\Delta z}{P}\right]_R \lambda_{A,v_z}\lambda_{A,\rho} = \left[\frac{r^2}{\nu}\right]_R \tag{70}$$

8.2.3. Energy

Starting from Equation (22), the parameters of interest are the fluid density and velocity, from Sections 8.2.1 and 8.2.2, and the fluid temperature, where the corresponding dimensionless form is $T^+ = T/T_0$ and (T_0 is the nominal fluid temperature):

$$\frac{\partial T^+}{\partial t} = \frac{\alpha}{r}\frac{\partial T^+}{\partial r} + \frac{\partial \alpha}{\partial r}\frac{\partial T^+}{\partial r} + \alpha\frac{\partial^2 T^+}{\partial r^2} + \frac{1}{T_0}\frac{\partial \alpha}{\partial z} + \alpha\frac{\partial^2 T^+}{\partial z^2} + \frac{\mu v_{z,0}}{\rho_0 T_0 c_P}\frac{1}{\rho^+}\frac{\partial v_z^+}{\partial r} - v_{z,0}v_z^+\frac{\partial T^+}{\partial z} \tag{71}$$

By applying Equation (59) to Equation (71)'s left- and right-hand sides, the scaled form is derived expressing fluid density and velocity from Equation (63) and fluid temperature and fluid-temperature agents of change as $\lambda_{A,T} = \frac{T^+_{target}}{T^+_{prototype}}$ and $\lambda_{B,T} = \frac{\frac{\partial T^+}{\partial t}_{target}}{\frac{\partial T^+}{\partial t}_{prototype}}$.

$$\lambda_{B,T} = \left[\frac{\alpha}{r}\frac{\partial T^+}{\partial r} + \frac{\partial \alpha}{\partial r}\frac{\partial T^+}{\partial r} + \alpha\frac{\partial^2 T^+}{\partial r^2} + \frac{1}{T_0}\frac{\partial \alpha}{\partial z} + \alpha\frac{\partial^2 T^+}{\partial z^2} + \frac{\mu v_{z,0}}{\rho_0 T_0 c_P}\frac{1}{\rho^+}\frac{\partial v_z^+}{\partial r} - v_{z,0}v_z^+\frac{\partial T^+}{\partial z}\right]_R \tag{72}$$

Following Equation (12) and the law of scaled ratios, the following is the derived relation:

$$\lambda_{B,T} = \left[\frac{\alpha}{r^2}\right]_R \lambda_{A,T} = \left[\frac{\alpha}{T_0\Delta z}\right]_R = \left[\frac{\alpha}{\Delta z^2}\right]_R \lambda_{A,T} = \left[\frac{\mu}{\rho_0 T_0 c_P r}\right]_R \frac{\lambda_{A,v_z}}{\lambda_{A,\rho}} = \left[\frac{v_{z,0}}{\Delta z}\right]_R \lambda_{A,v_z}\lambda_{A,T} \tag{73}$$

Using Equations (73) and (12), the time ratio is:

$$t_R = \left[\frac{r^2}{\alpha}\right]_R = \left[\frac{\Delta z^2}{\alpha}\right]_R = \left[\frac{\Delta z}{v_{z,0}}\right]_R \frac{1}{\lambda_{A,v_z}} \tag{74}$$

8.3. TEDS

As shown in Sections 8.1 and 8.2, the equations stated in Section 6 are in scaled form. Because the steps and results of this process are provided in [11], the steps are here omitted, and the results are presented in Sections 8.3.1 and 8.3.2. The mass scaled equations are the same as Section 8.2.1 and are omitted as well.

8.3.1. Scaled Momentum Equation

Although the form of Equation (28) is the same for Equation (21), the scaling conclusion for Equation (28) is not identical. For systems characterizing the TTSS fluid flow, the relation between pipe-outlet and thermocline-inlet fluid velocity are considered and applied as the following scaled equations:

$$\begin{aligned}
\lambda_{B,th} &= \left[\frac{\rho_{in} R_{in} v_{z,in,0} c_{P,in}}{\rho_{th} c_{P,th} R_{th}^2 \Delta z}\right]_R \lambda_{A,v_{z,in}} \lambda_{A,th} \\
\lambda_{B,th} &= \left[\frac{\rho_{in} R_{in} v_{z,in,0} c_{P,th} T_{in,0}}{\rho_{th} c_{P,th} R_{th}^2 \Delta z T_{th,0}}\right]_R \lambda_{A,v_{z,in}} \lambda_{A,in} \\
\lambda_{B,th} &= \left[\frac{\rho_{in} R_{in} v_{z,in,0} c_{P,th} T_{out,0}}{\rho_{th} c_{P,th} R_{th}^2 \Delta z T_{th,0}}\right]_R \lambda_{A,v_{z,in}} \lambda_{A,out}
\end{aligned} \tag{75}$$

where $\lambda_{B,th}$ is the middle axial-thermocline fluid-temperature agents of change scaled form. $\lambda_{A,th}$ is the middle axial-thermocline fluid-temperature scaled form. $T_{th,0}$ is the nominal-middle axial-thermocline fluid temperature. $\lambda_{A,in}$ is the thermocline inlet-temperature scaled form. $T_{in,0}$ is the nominal thermocline inlet temperature. $\lambda_{A,v_{z,in}}$ is the thermocline inlet velocity scaled form. $v_{z,in,0}$ is the nominal thermocline inlet velocity. $\lambda_{A,T_{out,0}}$ is the thermocline outlet-temperature scaled form, and T_{out} is the nominal thermocline outlet temperature.

8.3.2. Scaled Energy Equation

The equation set shown in Equation (33) is a unique form describing energy exchange between Therminol-66 and alumina beads, heat loss, and axial heat transfer. The following is the scaled form:

$$\begin{aligned}
\lambda_{B,th} &= \left[\frac{k T_{w,0}}{\rho_{th} \varepsilon R_{th}^2 T_{th,0}}\right]_R \frac{\lambda_{A,T_w}}{\lambda_{A,r}} \\
\lambda_{B,th} &= \left[\frac{k T_{amb,0}}{\rho_{th} \varepsilon R_{th}^2 T_{th,0}}\right]_R \frac{\lambda_{A,T_{amb}}}{\lambda_{A,r}}
\end{aligned} \tag{76}$$

where λ_{A,T_w} is the wall-temperature scaled form, $T_{w,0}$ is the nominal wall temperature, $\lambda_{A,r}$ is the wall-thickness scaled form, $\lambda_{A,T_{amb}}$ is the ambient-temperature scaled form, and $T_{amb,0}$ is the nominal ambient wall temperature.

8.4. HTSE

Similar to Section 8.3, the steps and results of this process are provided in [12]. The steps are omitted, and the results are presented in Sections 8.4.1–8.4.5.

8.4.1. Reversible Overvoltage

Due to the first-order delay constants of each element for pressure control and the corresponding Laplace variable, a neat scaled form is not feasible. However, by treating the coupled terms as one parameter, the derived scaled relation is the following:

$$\lambda_{B,V} = \left[\ln \left(\frac{\left[\left(\frac{\pi_{ca}+1}{\pi_{ca}} \right)^{\lambda} \frac{1}{1+s\tau_{H_2}} \right] \left[\left(\frac{\pi_{an}+1}{\pi_{an}+P_{O_2,in}} \right)^{\lambda} \frac{1}{1+s\tau_{O_2}} \right]}{\left[\left(\frac{\pi_{ca}-1}{\pi_{ca}} \right)^{\lambda} \frac{1}{1+s\tau_{H_2O}} \right]} \right)^{\frac{\bar{T}_0}{V_0}} \right]_R \lambda_{B,\bar{T}_0}, \qquad \lambda_{A,V} = \left[\frac{\bar{T}_0}{V_0} \right]_R \lambda_{A,\bar{T}} \tag{77}$$

where $\lambda_{B,V}$ is the stack-voltage agents-of-change scaled form, $\lambda_{B,\bar{T}_0}$ is the stack average temperature agents-of-change scaled form, $\lambda_{A,V}$ is the stack-voltage parameter-of-interest scaled form, V_0 is the nominal stack voltage, $\bar{T}_0$ is the nominal stack average temperature, and $\lambda_{A,\bar{T}}$ is the stack-average-temperature parameter-of-interest scaled form.

8.4.2. Ohmic Overvoltage

Acknowledging that the reference-area specific resistance correlation limits scaling to its valid range, the following are the ohmic overvoltage scaling relations:

$$\lambda_{A,V} = \left[\frac{I\bar{T}_0 e^{\frac{10,300}{\bar{T}}}}{AV_0} \right]_R \tag{78}$$

where $\lambda_{A,V}$ is the stack voltage parameter of interest scaled form.

8.4.3. Activation Overvoltage

Due to approximations using the Butler–Volmer equation, scaling is restricted to its valid range as well. The following is the activation overvoltage scaling relations:

$$\lambda_{B,V} = \left[\frac{\bar{T}_0}{V_0} \sinh^{-1} \left(\frac{I}{2I_{ex,xx}} \right) \right]_R \lambda_{B,\bar{T}} \tag{79}$$

where the subscript xx in hyperbolic sine can be ca and an, which would indicate either cathode or anode.

8.4.4. Stack Thermal Dynamics

Given the multiple terms characterizing energy source, sink, inlet, and outlet, numerous scaled forms can be determined:

$$\begin{aligned} \lambda_{B,\bar{T}} &= \frac{n_c I \Delta H_0}{\bar{T}_0 C_{P,SOEC}} \lambda_{A,\Delta H} = \frac{P_{heat}}{\bar{T}_0 C_{P,SOEC}} \lambda_{A,P_{heat}} \\ &= \left[\frac{c_{P,yy} n_c I \pi_{xx} P_{yy,in} T_{out,0} \text{ or } T_{in,0}}{\bar{T}_0 C_{P,SOEC} P_{zz,in}} \right]_R \lambda_{A,T_{out} \text{ or } T_{in}} \end{aligned} \tag{80}$$

where $\lambda_{A,\Delta H}$ represents the enthalpy-difference parameter-of-interest scaled form, ΔH_0 the nominal enthalpy change, $\lambda_{A,P_{heat}}$ the stack heater-power parameter-of-interest scaled form, $P_{heat,0}$ the nominal stack heat power, $\lambda_{A,T_{in}}$ the stack inlet-temperature parameter-of-interest scaled form, $T_{in,0}$ the nominal stack-inlet temperature, $\lambda_{A,T_{out,0}}$ the stack outlet-temperature parameter-of-interest scaled form, and T_{out} the nominal stack-outlet temperature. The subscripts xx, yy, and zz represent the available patterns of Equation (80). When xx is ca, the possible characters for yy are H_2 and H_2O, and zz is H_2O. When xx is an, the remaining characters of yy are O_2 and N_2, and zz is O_2.

8.4.5. Preheater Thermal Dynamics

As stated in Section 8.4.4, multiple terms create numerous scaled forms. Equation (78) shows the possible preheater thermal-dynamics scaled forms:

$$\lambda_{B,T_{in}} = \frac{1}{C_{P,pre} T_{in}} \lambda_{A,P_{heat,pre}} = \left[\frac{c_{P,yy} n_c I \pi_{xx} P_{yy,in} (1-\epsilon) T_{in} \text{ or } T_{ww}}{T_{in} C_{P,SOEC} P_{zz,in}} \right]_R \lambda_{A,T_{in} \text{ or } T_{ww}} \tag{81}$$

where $\lambda_{B,T_{in}}$ is the stack inlet-temperature agents-of-change scaled form, $\lambda_{A,P_{heat,pre}}$ is the preheater-power parameter-of-interest scaled form, $P_{heat,pre}$ is the nominal preheater power, $\lambda_{A,T_{steam}}$ is the steam-temperature parameter-of-interest scaled form, $T_{steam,0}$ is the nominal steam temperature, $\lambda_{A,T_{amb}}$ is the ambient-temperature parameter-of-interest scaled form, and $T_{amb,0}$ is the nominal ambient temperature. The subscripts xx, yy, zz, and ww represent the available patterns of Equation (81). When xx is ca, the possible characters for yy are H_2 and H_2O, zz is H_2O, and ww is $steam$. When xx is an, the remaining characters of yy are O_2, N_2, zz is O_2, and ww is amb.

9. Connective System Scaling

When emulating an IES, each component included represents a portion that enables flexible operation to load balance and maximize assets while accommodating the market's daily demand. Furthermore, if a laboratory-scale IES emulation is to be operated to reflect industry-scale processes, the laboratory IES entirely must be upscaled. This can be performed by (1) setting the upscale range, (2) determining scaling objectives, (3) deriving scaled equations, (4) calculating scaled ratios, and (5) applying scaling analysis. This does not imply that geometrical characteristics or size of components are required to be altered. Rather, it is the decision of scaling objectives that determine the necessity of such actions. For this analysis, the chain of assumptions and scaling objectives are addressed in Section 11.

For the last stage in Step 3, this section is dedicated to determine how each system's scaling will affect surrounding systems in a TEDS-HTSE IES setup.

9.1. Connect Heat Exchanger Tube-Side and Pipe Scaling

The heat-exchanger duty-load tube-outlet temperature equation shown in Equation (61) can be reorganized to be explicit as to tube-outlet temperature:

$$\lambda_{A,T_{tube,out}} = \left[\frac{\rho v_{T,0} Q_0 \times ID^2}{\dot{m} L N_P F_T \times OD}\right]_R \left[\ln\left(\frac{T_{shell,in} - T_{tube,in}}{T_{shell,out} - T_{tube,out}}\right)\right]_R \left[\frac{1}{T_{tube,out,0}}\right]_R \left[\frac{A_i}{A_o}\left(\frac{k_w}{OD - ID}\right)\right]_R \lambda_{A,v_T} \lambda_{A,Q} \tag{82}$$

By multiplying Equation (73) with the time ratio, the pipe fluid-temperature parameter-of-interest scaled form is:

$$\lambda_{A,T} = \lambda_{B,T} t_R = \left[\frac{\mu}{\rho c_P r}\right]_R \lambda_{A,v_z} t_R \tag{83}$$

Because the heat-exchanger tube outlet and pipe inlet are at the same location, their temperature-scaling ratio is equivalent and acts as the connective aspect between the heat exchanger and piping:

$$\lambda_{A,T} = \lambda_{A,T_{tube,out}} \tag{84}$$

9.2. Connect Pipe and TTSS Scaling

The TTSS energy-balance-based scaled equation, shown in Equation (75), can be reorganized to be explicit as to inlet velocity:

$$\lambda_{A,v_{z,in}} = \left[\frac{\rho_{th} c_{P,th} R_{th}^2 \Delta z}{\rho_{in} R_{in} v_{z,in,0} c_{P,in}}\right]_R \frac{1}{t_R} \tag{85}$$

where $\lambda_{B,th}/\lambda_{A,th}$ is converted to $1/t_R$. By multiplying Equation (68) with the time ratio, the pipe fluid-velocity parameter-of-interest scaled form is:

$$\lambda_{A,v_z} = \lambda_{B,v_z} t_R = \left[\frac{P}{\Delta z}\right]_R \frac{t_R}{\lambda_{A,\rho}} \tag{86}$$

This inlet velocity is actually the piping outlet velocity into the TTSS, and the scaled forms are equivalent:

$$\lambda_{A,v_{z,in}} = \lambda_{A,v_z} \tag{87}$$

9.3. Connect TTSS and Pipe Scaling

The TTSS energy-balance-based scaled equation, shown in Equation (75), can be reorganized to be explicit as to outlet velocity:

$$\lambda_{A,v_{z,out}} = \left[\frac{\rho_{th} c_{P,th} R_{th}^2 \Delta z}{\rho_{out} R_{out} v_{z,out,0} c_{P,out}}\right]_R \frac{1}{t_R} \tag{88}$$

This outlet velocity is actually the piping inlet velocity out the TTSS, and the scaled forms are equivalent:

$$\lambda_{A,v_z} = \lambda_{A,v_{z,out}} \tag{89}$$

9.4. Connect Pipe and Helical Steam Generator Tube-Side Scaling

The helical steam generator acts as the media transferring heat from TEDS to HTSE. When considering from the TEDS side, the helical tubing carries the hot therminol-66 fluid. Thus, the steam generator duty-load tube-inlet temperature equation shown in Equation (61) can be reorganized to be explicit to tube-inlet temperature:

$$\lambda_{A,T_{tube,in}} = \left[\frac{\rho v_{T,0} Q_0 \times ID^2}{\dot{m} L N_P F_T \times OD}\right]_R \left[\ln\left(\frac{T_{shell,in} - T_{tube,in}}{T_{shell,out} - T_{tube,out}}\right)\right]_R \left[\frac{1}{T_{tube,in,0}}\right]_R \left[\frac{A_i}{A_o}\left(\frac{k_w}{OD - ID}\right)\right]_R \lambda_{A,v_T} \lambda_{A,Q} \tag{90}$$

The equation for pipe fluid temperature is provided in Equation (83). Since the steam generator tube inlet and pipe outlet are at the same location, their temperature scaling ratio are equivalent and act as the connective aspect between the steam generator and piping:

$$\lambda_{A,T_{tube,in}} = \lambda_{A,T} \tag{91}$$

9.5. Connect Helical Steam Generator Shell-Side and Pipe Scaling

When considered from the HTSE side, the helical shell transports the HTSE feedwater. Thus, the steam-generator duty-load shell-outlet temperature equation shown in Equation (61) can be reorganized to express explicitly the shell-outlet temperature:

$$\lambda_{A,T_{shell,out}} = \left[\frac{\rho v_{T,0} Q_0 \times ID^2}{\dot{m} L N_P F_T \times OD}\right]_R \left[\ln\left(\frac{T_{shell,in} - T_{tube,in}}{T_{shell,out} - T_{tube,out}}\right)\right]_R \left[\frac{1}{T_{shell,out,0}}\right]_R \left[\frac{A_i}{A_o}\left(\frac{k_w}{OD - ID}\right)\right]_R \lambda_{A,v_T} \lambda_{A,Q} \tag{92}$$

The equation for the pipe-fluid temperature is provided in Equation (83). Because the steam-generator shell outlet and pipe inlet are at the same location, their temperature-scaling ratios are equivalent and act as the connective aspect between the steam generator and piping:

$$\lambda_{A,T} = \lambda_{A,T_{shell,out}} \tag{93}$$

9.6. Connect Pipe and Preheater Scaling

The trim-heater power-differential inlet-temperature equation is Equation (81), and it can be reorganized to be explicit to the stack-inlet temperature agents of change. By multiplying the time ratio, the parameter-of-interest scaled form is:

$$\lambda_{A,T_{in}} = \lambda_{B,T_{in}} t_R = \left[\frac{1}{C_{P,pre} T_{in,0}}\right]_R \lambda_{A,P_{heat,pre}} t_R \tag{94}$$

Because all systems are bounded by the same time ratio, using Equations (63) and (92) reveals the relationship between the inlet piping and preheater:

$$t_R = \left[C_{P,pre} T_{in,0}\right]_R \frac{\lambda_{A,T_{in}}}{\lambda_{A,P_{heat,pre}}} = \left[\frac{\rho c_p r}{\mu}\right]_R \frac{\lambda_{A,T}}{\lambda_{A,v_z}} \tag{95}$$

Thus, the preheater parameter-of-interest scaled form is:

$$\lambda_{A,P_{heat,pre}} = \left[\frac{\mu}{\rho c_P r}\right]_R \left[C_{P,pre} T_{in,0}\right]_R \frac{\lambda_{A,T_{in}} \lambda_{A,v_z}}{\lambda_{A,T}} \tag{96}$$

9.7. Connect Preheater and Stack Scaling

Because the scaling-form relationship between the preheater and SOEC stack is already established, no further derivation is required. Equation (92) should suffice as the connective relation.

9.8. Connect Stack and Pipe Scaling

The water-specific heat-capacity difference differential equation is in Equation (80), and it can be reorganized to be explicit to the stack-outlet temperature parameter-of-interest scaled form:

$$\lambda_{A,T_{in}} = \left[\frac{\bar{T}_0 C_{P,SOEC}}{c_{P,SOEC} n_c I \pi_{ca} T_{in,0}}\right]_R \lambda_{B,\bar{T}} \tag{97}$$

The equation for pipe-fluid temperature is provided in Equation (83). Because the stack outlet and pipe inlet are at the same location, their temperature-scaling ratio is equivalent and acts as the connective aspect between the SOEC stack and piping:

$$\lambda_{A,T} = \lambda_{A,T_{in}} \tag{98}$$

9.9. Connect Pipe and Helical Steam-Generator Shell-Side Scaling

When considered from the HTSE side, the helical shell transports the HTSE feedwater, as stated previously. Thus, the steam-generator duty-load shell-inlet temperature equation shown in Equation (61) can be reorganized to be explicit to shell inlet temperature:

$$\lambda_{A,T_{shell,inlet}} = \left[\frac{\rho v_{T,0} Q_0 \times ID^2}{\dot{m} L N_P F_T \times OD}\right]_R \left[\ln\left(\frac{T_{shell,in} - T_{tube,in}}{T_{shell,out} - T_{tube,out}}\right)\right]_R \left[\frac{1}{T_{shell,in,0}}\right]_R \left[\frac{A_i}{A_o}\left(\frac{k_w}{OD - ID}\right)\right]_R \lambda_{A,v_T} \lambda_{A,Q} \tag{99}$$

The equation for pipe-fluid temperature is provided in Equation (83). Because the steam-generator shell inlet and pipe outlet are at the same location, their temperature-scaling ratio is equivalent and acts as the connective aspect between the steam generator and piping:

$$\lambda_{A,T_{shell,in}} = \lambda_{A,T} \tag{100}$$

10. TEDS and HTSE Test Case

For the scaling validation of TEDS and HTSE scaling efforts, simulation or experimental data are required. Because the maintenance of TEDS and HTSE is ongoing, the Modelica-language-based system-modeling tool Dymola [30], a tool for the modeling and simulation of integrated and complex systems, is used to generate data. The Modelica models for TEDS and HTSE are developed from previous INL IES efforts, shown in Section 10.1, and can be found in [17,31]. The simulation results shown in Section 10.2 are the generated simulation data and are based on model runnability. These results are post-processed to determine the projected case's initial and boundary conditions and data, using derived scaling equations from Sections 6 and 7.

10.1. Dymola Models

10.1.1. TEDS

TEDS includes several components: a single-tank packed-bed thermocline energy-storage tank, an ethylene glycol heat exchanger, and a Chromalox heater are among them. A schematic of the whole TEDS Modelica model is seen in Figure 4 [31].

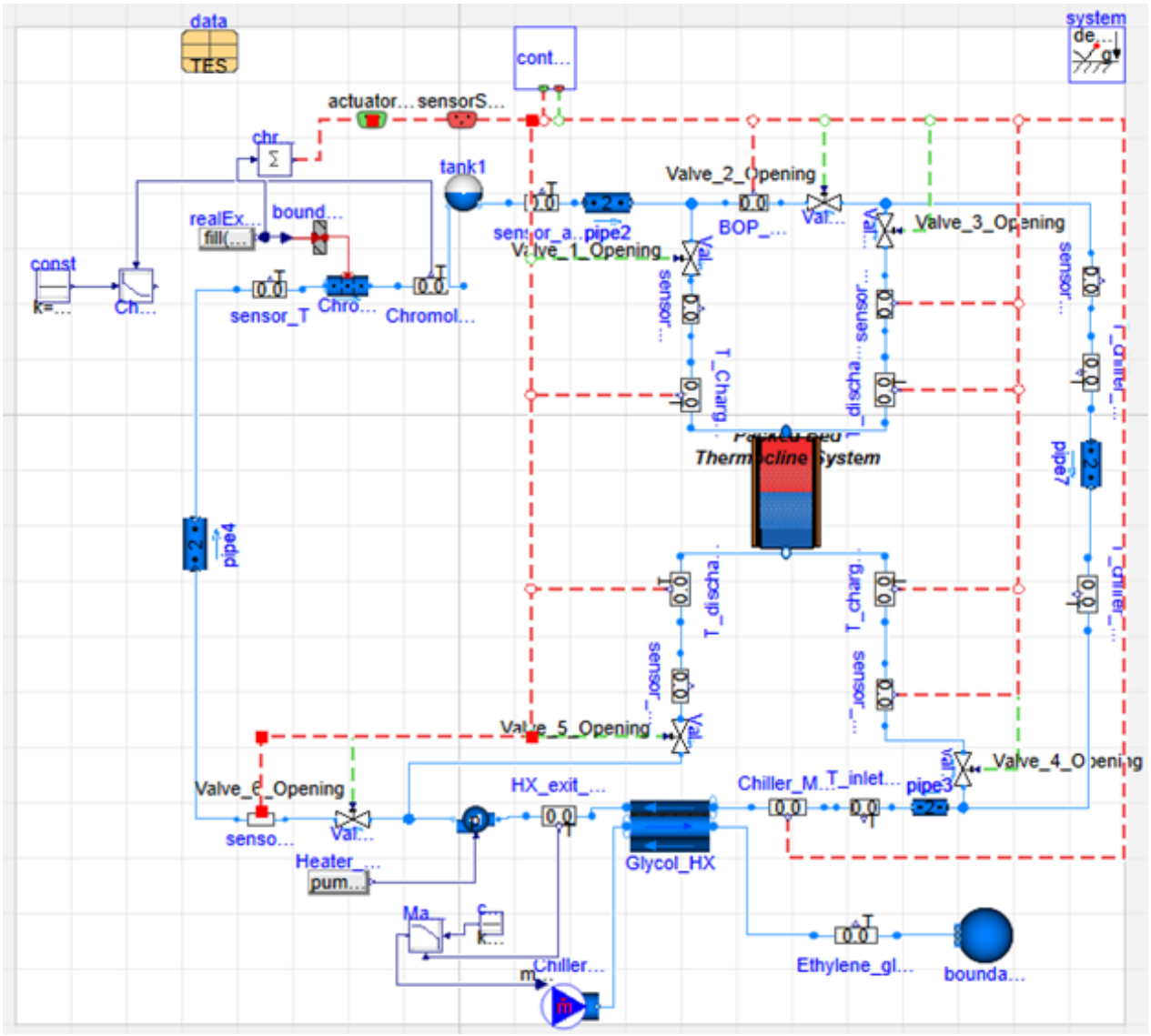

Figure 4. Overview of TEDS schematic [31].

A single-tank packed-bed thermocline tank is used in TEDS for energy storage. A thermocline system uses hot and cold fluid, separated by a thin thermocline region, to store heat. The position of the thermocline moves depending on whether charging or discharging occurs. Hot fluid is pumped into the top of the tank, and cold fluid exits the bottom of the tank during the charging mode. During the discharge mode, cold fluid enters the bottom of the tank, and hot fluid exits from the top of the tank. The thermocline system is split into 200 axial nodes, each of which incorporates both a solid and fluid component. The inlets to and outlets from the thermocline can be seen in Figure 5, along with sensors for the mass-flow rate and temperature of the inlet and outlet during both charging and discharging modes. The thermocline system can be seen in Figure 6, along with the wall and insulation components. The nodal representation of i = 1 to i = N can be seen here, with this model having 200 nodes. It can store up to 200 kW thermal. The filler material for the single-tank packed-bed thermocline is 1/8 in. diameter Al_2O_3 (alumina) beads. Radial heat loss occurs, in addition to axial heat loss, through the tank walls and insulation. Heat losses are calculated via Fourier's law of heat conduction, seen below. The built-in Modelica models for conduction in cylinders are used.

$$q'' = -k\frac{dT}{dx} \tag{101}$$

The thermocline system is modeled using modified Schumann equations. More information about the Schumann equations can be found at [24,32,33]. Table 1 shows the parameters used in the TEDS model.

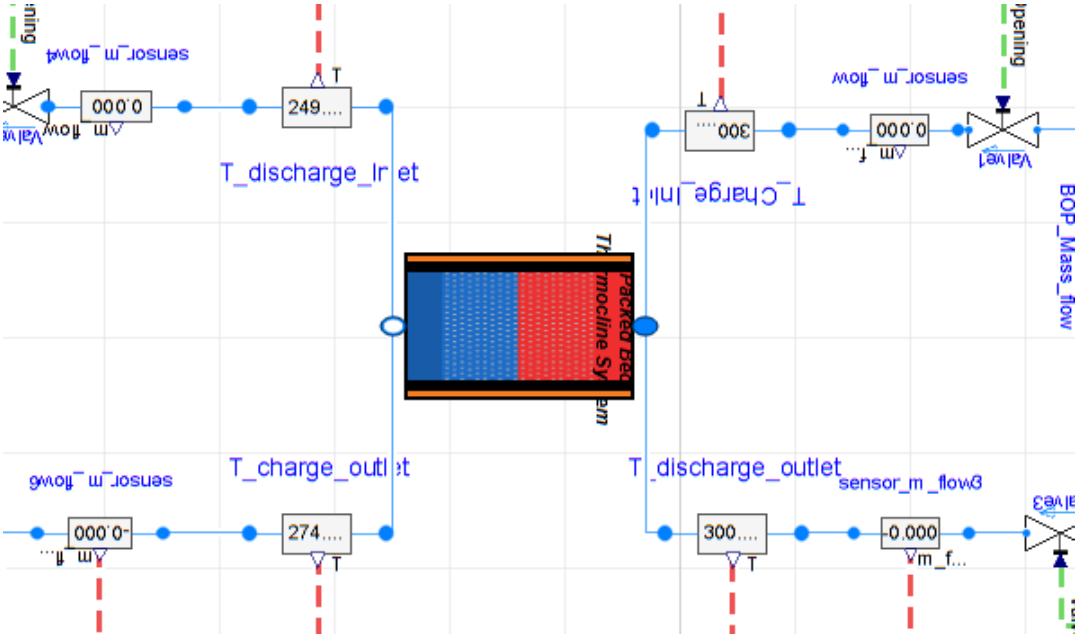

Figure 5. Enlarged Thermocline in TEDS model as shown in Figure 4.

Table 1. Design Specification for TEDS [31].

Parameter	Value
Fluid Material	Therminol-66
Filler Material	Alumina
Wall Material	Stainless Steel 304
Insulation Material	Foamglass One
Porosity	0.25
Filler Diameter	0.00317 m (1/8 in.)
Tank Height	14.6 m
Tank Radius	7.3 m
Ambient Temperature	293 K
Nodes	200
Wall Thickness	0.051 m
Insulation Thickness	0.102 m
Change Incoming Temperature	598 K
Discharge Incoming Temperature	498 K
Maximum Heater Power	200 kW
Nominal Full Heater Output	175 kW

The Chromalox heater is the heat source for the loop in this model. The heater and its inputs and outputs can be seen in Figure 7. The Chromalox heater is modeled using a multitransfer surface pipe. The medium is Therminol-66.

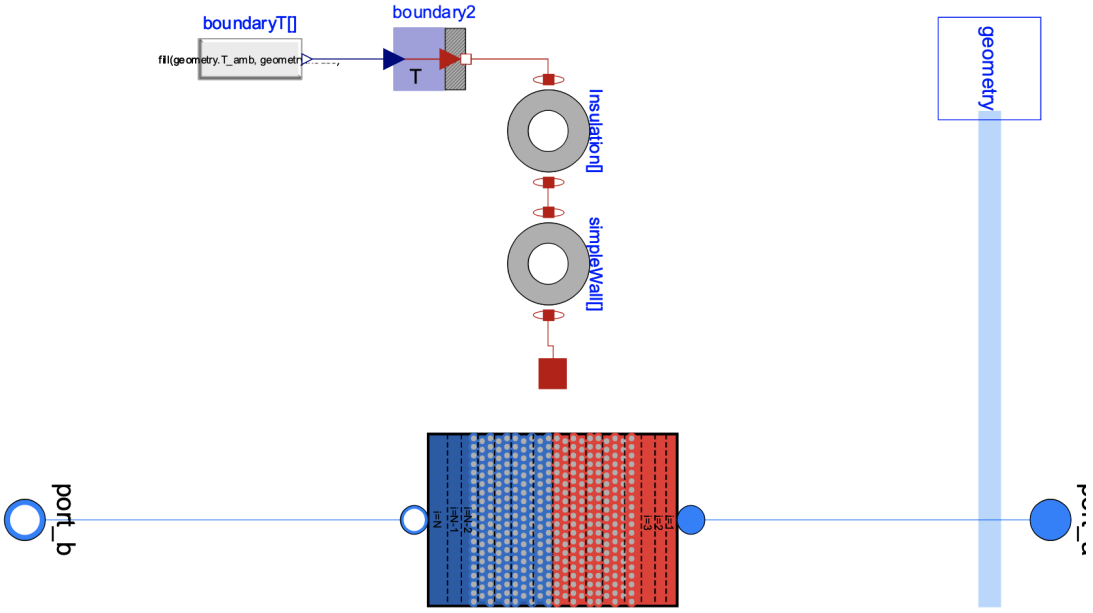

Figure 6. The enlarged Modelica model for the single-tank packed-bed thermocline tank shown in Figure 4.

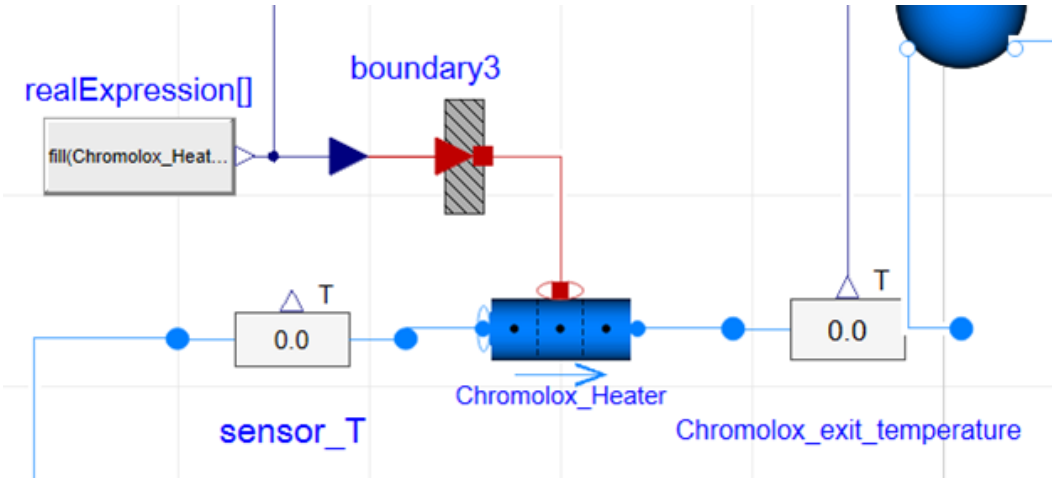

Figure 7. The Chromalox heater shown in Figure 4.

The ethylene glycol heat exchanger is a generic distributed heat exchanger that acts as a heat-sink/heat-control unit in the loop. A schematic of the ethylene glycol heat exchanger can be seen in Figure 8. This type of heat exchanger has no inlet or outlet plenum considerations and is a shell-and-tube heat exchanger. It is a generic heat exchanger with discretized fluid and wall volumes. The tube side contains ethylene glycol and the shell side, Therminol-66. The tube material for the heat exchanger is set to stainless steel 316. The heat transfer on both the tube and shell sides is calculated using a simple Dittus–Boelter correlation, seen below. The correction factors are adjusted to meet predetermined heat-transfer characteristics.

$$Nu = A \times Re^B \times Pr^C \tag{102}$$

There are several operational modes controlled by the valves seen in Figure 9. Valve 2 controls the heat source to load, Valves 1 and 4 control the flow during charging mode, and

Valves 3 and 5 control the system during discharge mode. More information on the control strategies can be found in [31,32].

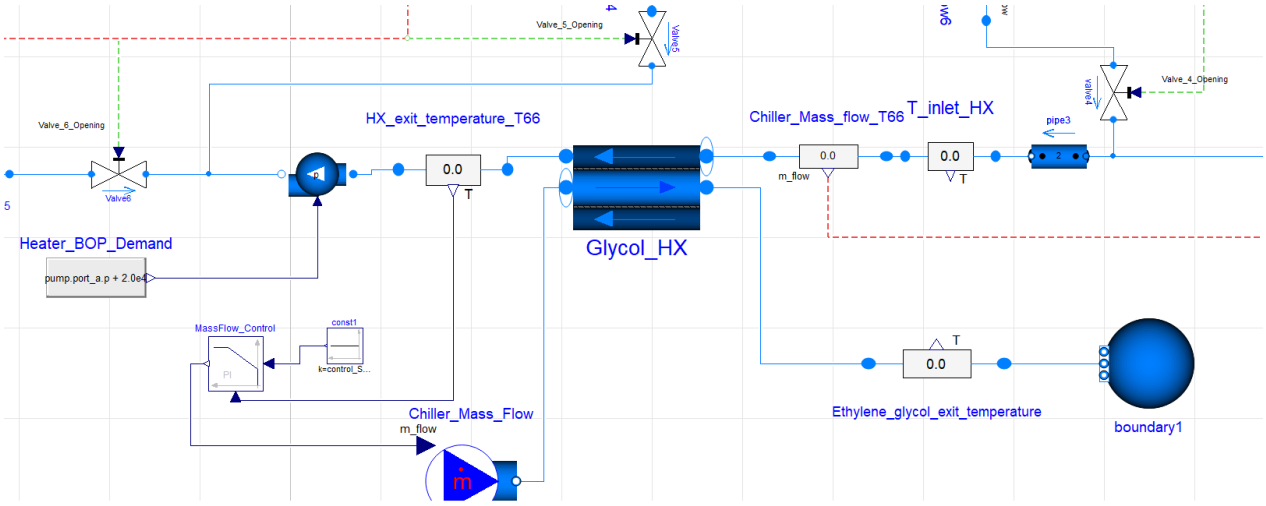

Figure 8. Enlarged Glycol heat exchanger as shown in Figure 4.

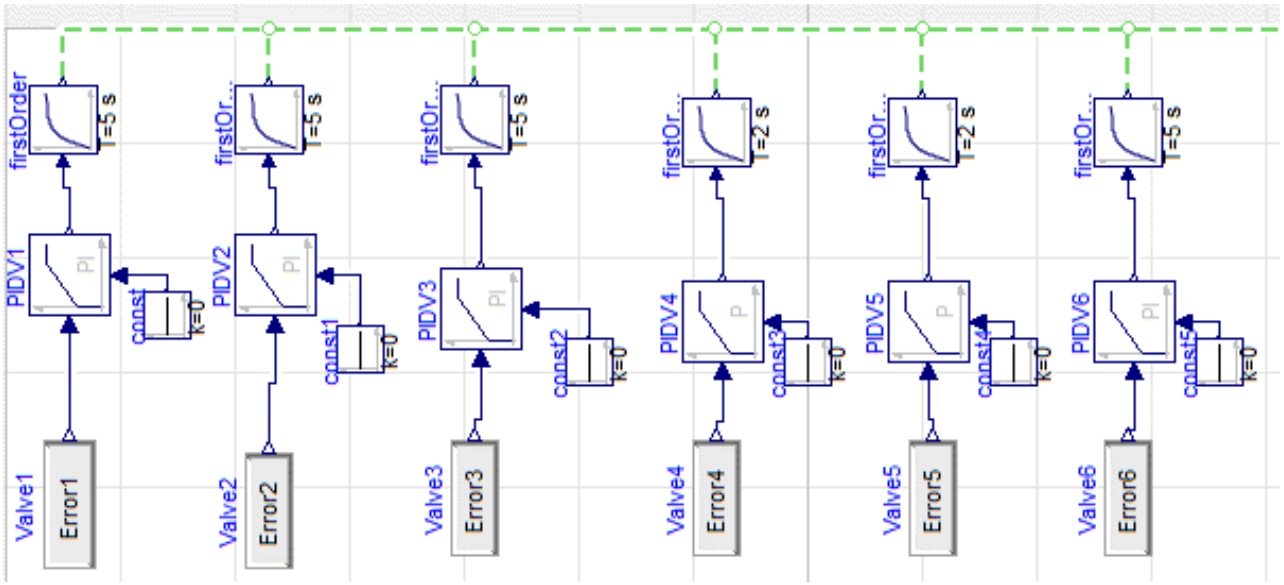

Figure 9. Internal control system interface of valves in TEDS.

10.1.2. HTSE

The individual components of the HTSE are the SOEC, the recuperative heat exchangers, a hydrogen recycler, and a condenser. The full Dymola model of the HTSE can be seen in Figure 10 [17]. The figure includes all of the modeling components inside the HTSE system and depicts connections to the outside via ports, such as both the inlet- and outlet-air ports, the steam-inlet port, the water-outlet port, the hydrogen-outlet port, and the electrical-inlet port. The SOEC is where steam is split into hydrogen. Other components show heat transfer of the inlet and outlet stream and how the inlet steam contribution is maintained. Condenser components can be seen in the dashed green box in Figure 10. The hydrogen recycler component is in the purple box, and the SOEC component is seen in the orange-dotted box in Figure 10. The SOEC is composed of 12 stacks, each of which contains 65 cells, for a total of 780 cells in the SOEC. The SOEC base model is shown in Figure 11, which shows the basic cathode and anode side of the SOEC.

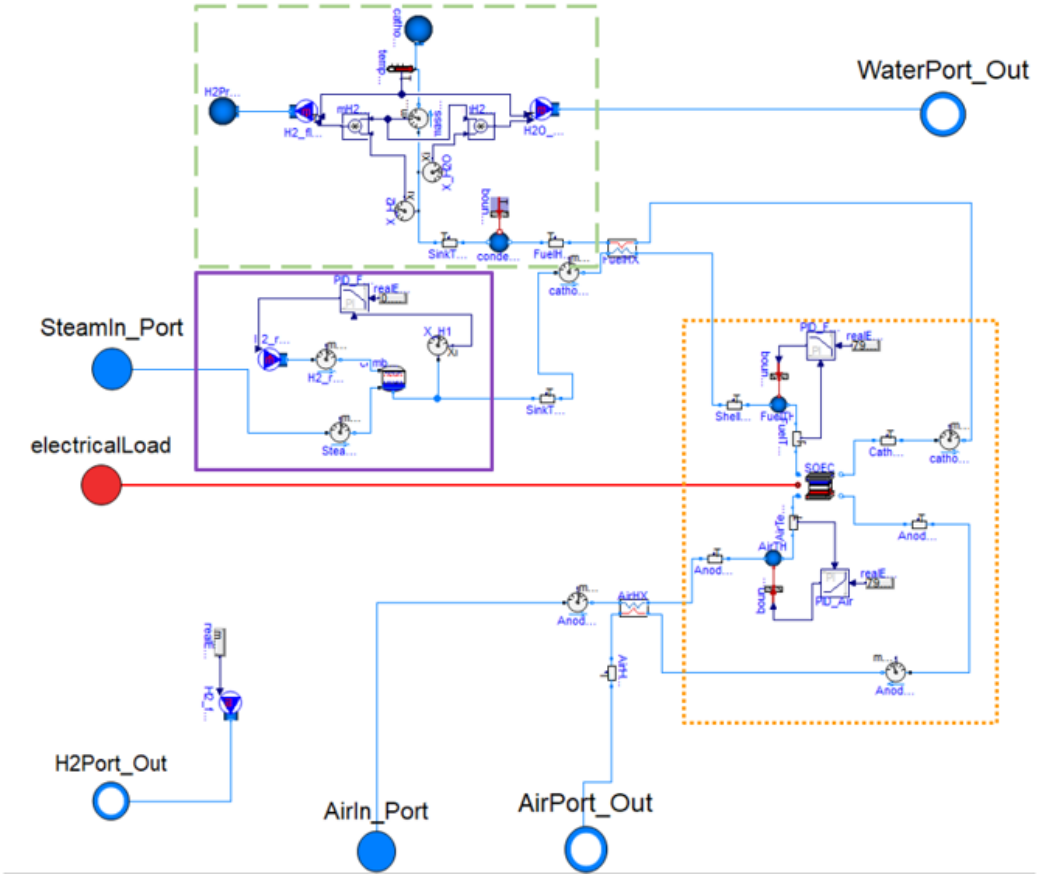

Figure 10. The Modelica model of HTSE [17]. The box with the dashed green line represents the condenser. The box with the orange-dotted line is the SOEC, and the purple box is the recycler.

The condenser is modeled as an ideal component splitter, which allows the individual species to be split in the incoming stream. The condenser allows for cooling of the hydrogen and condensation of the steam. This allows them both to cool to 313 K. The component splitter measures the temperature and mass fractional flow of the individual species and provides those to two separate mass flow sources. The flow of the pure species goes to the outlet boundary ports. These outlet flows are the produced hydrogen and condensed water.

Ten percent of the gas stream must be hydrogen in order to maintain a reducing environment for the cathode side of the SOEC. The hydrogen-recycler component is made up of an ideal combiner, a proportional–integral–derivative (PID) controller, a hydrogen mass-flow source, and mass-flow-rate sensors. The PID controller controls the hydrogen mass-flow source so that a 90% H_2O/10% H_2 molar fraction is maintained. The combiner mixes the incoming streams. In this case, the mixed streams are steam and hydrogen.

The HTSE model must be connected to a direct current (DC) power source and fluid-boundary sources and ports, which can be seen in Figure 12. Table 2 shows the parameters used in the HTSE model.

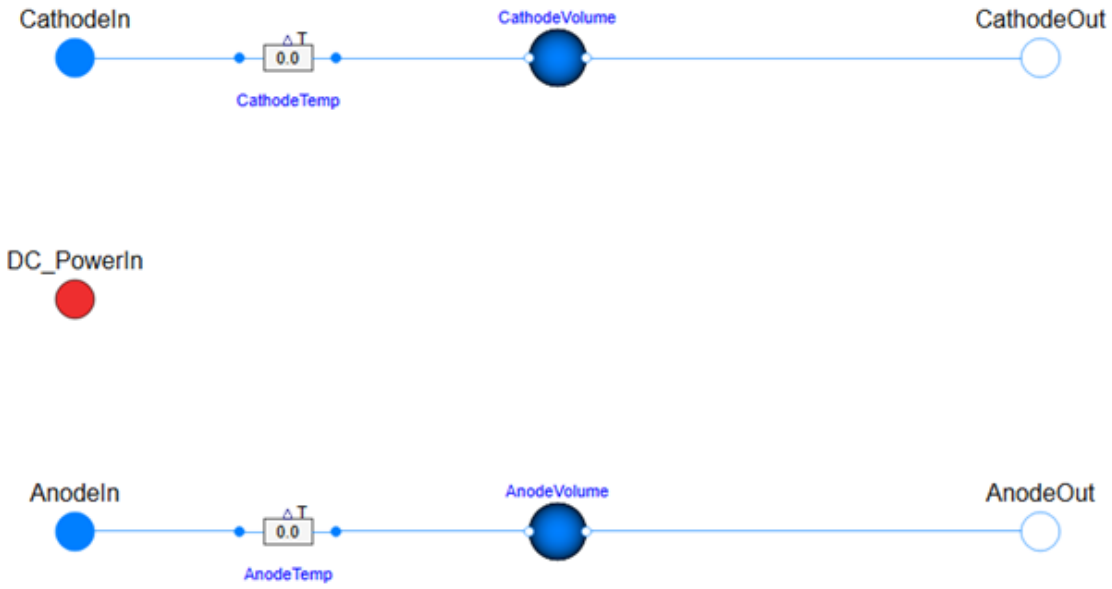

Figure 11. Dymola SOEC Base Model [17].

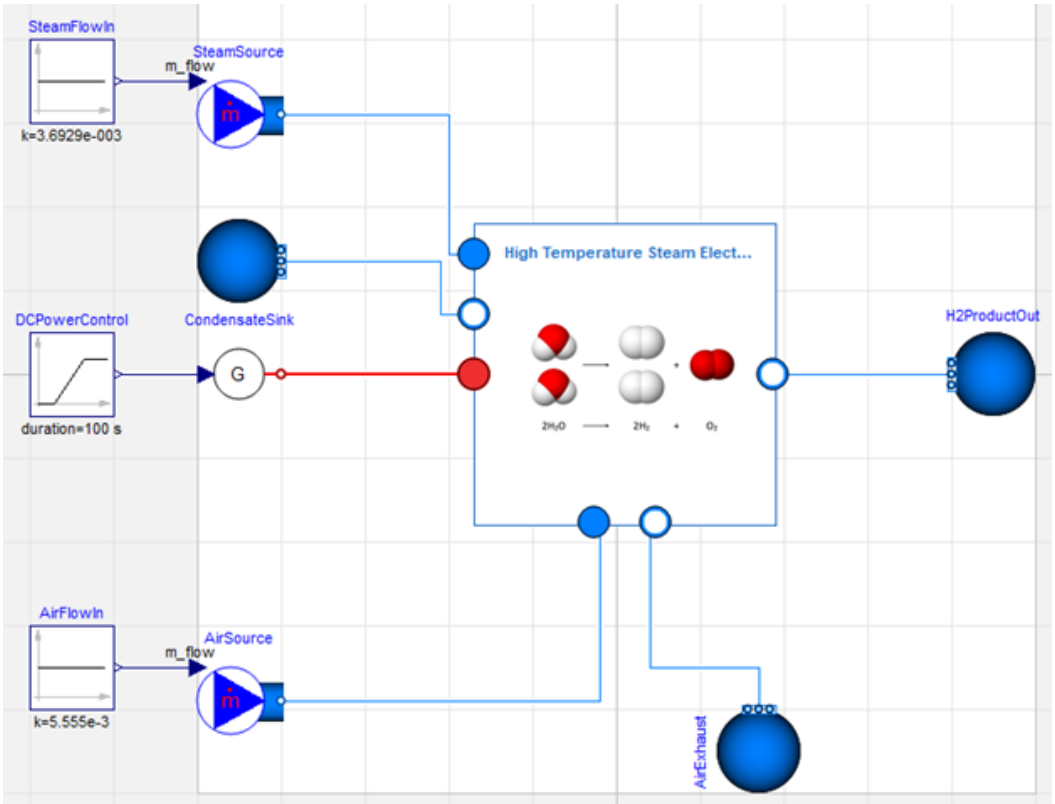

Figure 12. Dymola Full HTSE Model [17].

Table 2. Design specification of HTSE.

Parameter	Value	Units
Stack cell width	0.10526	m
Stack cell length	0.10526	m
Active cell area	0.01108	m^2
Active cell area in cm^2	110.797	cm^2
Number of cells per stack	65	
Number of stacks	12	
Total number of cells	780	
Thermo-neutral voltage	1.283	V
Area specific resistance	1.3	cm^2
Start value of inlet pressure at cathode	103,299.8	Pa
Start value of inlet pressure at anode	103,299.8	Pa
Stack temperature	1063	K
Open circuit voltage (OCV)	0.93	V
Total stack voltage	1000.74	V

10.2. Test Case Simulation Results

10.2.1. TEDS

The TEDS test case had a maximum power of 175 kW thermal for the thermal-energy system (i.e., the thermocline storage tank). The maximum Chromalox heater power was 200 kW thermal. The maximum temperature was set to 598 K, and the minimum temperature was set to 498 K. The relative heater demand (i.e., whether the heater is on or off) can be seen in Table 3. The demand from the balance of plant (BOP) is given as a function of time in Table 4. It was run for a 5-h (18,000 s) cycle, during which both charge and discharge occurred. The heater turned off at 9600 s, and the system switched from the charging to the discharging mode (see Figure 13b). The temperature curves for the test case can be seen in Figures 13a and 14a,b. The mass-flow rates for the inlet of the charge line, outlet of the charge line, inlet of the discharge line, and outlet of the discharge line can be seen in Section 12.1. The power provided by the Chromalox heater can be seen in Figure 13b.

Table 3. The normalized relative heater demand in terms of 0 (off) or 1 (on).

Time (s)	Relative Heater Demand
0	1
1800	1
3600	1
4800	1
7200	1
9000	1
9600	1
10,800	0
12,000	0
14,400	1
18,000	1

Table 4. BOP relative demand as a percentage of the heater power.

Time (s)	BOP Relative Demand
0	100
1800	100
3600	0
4800	0
7200	0
9000	0
9600	100
10,800	140
12,000	140
14,400	100
18,000	100

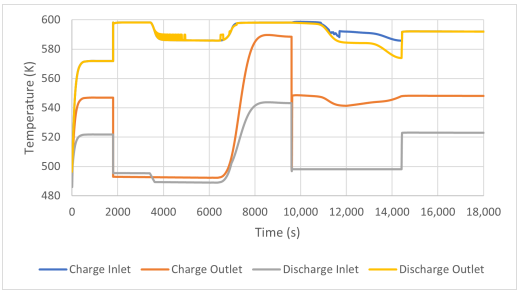

(**a**) Thermocline temporal temperature profile.

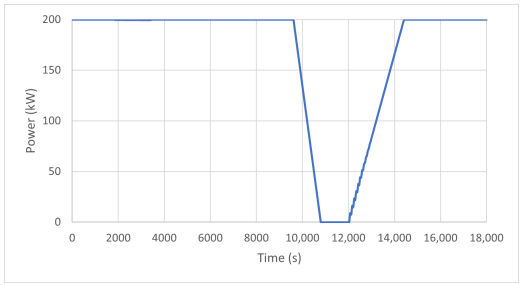

(**b**) Chromalox heater power.

Figure 13. The thermocline temporal temperature profile and the corresponding heat power.

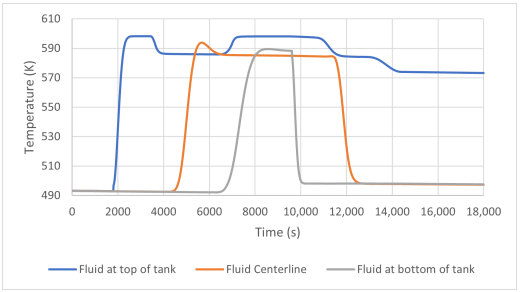

(**a**) The temperature at several locations inside the thermocline tank.

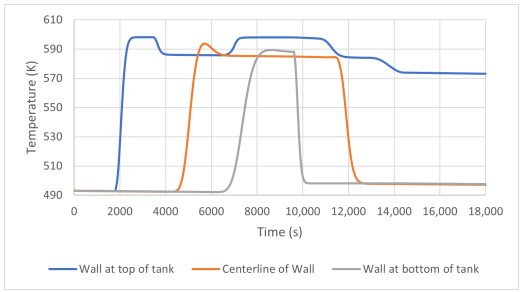

(**b**) The temperature at several locations at the thermocline wall.

Figure 14. The thermocline centerline temporal temperature profile.

10.2.2. HTSE

The HTSE test case had a thermo-neutral voltage of 1.283 V. The stack temperature was 1063 K. The input values for the anode and cathode mass flow rates can be seen in Table 5. The simulations were run for 1000 s and showed a transient system that is modeled as a steady state. The results can be seen in Table 6.

Table 5. Start values for the parameters that change in the HTSE model.

Parameter	Start Value
H_2/H_2O inlet mass flow rate of the cathode	0.003741667 kg/s
H_2/H_2O outlet mass flow rate of the cathode	0.0017861 kg/s
H_2/H_2O inlet mass flow rate of the cathode	0.003741667 kg/s
N_2/O_2 inlet mass flow rate of the anode	0.005556 kg/s
N_2/O_2 outlet mass flow rate of the anode	0.0075117 kg/s

Table 6. Results for the outlet parameters of interest for the HTSE test case. There are three output parameters whose values change between 500 and 600 s; the ones that change are the stack inlet temperature, the stack outlet temperature, and the calculated current. All the other parameters are the same for the whole simulation time of 1000 s.

Output Parameter	Value
Stack inlet temperature (<500 s)	984.8 K
Stack outlet temperature (<500 s)	1063.2 K
Ambient temperature	293.1 K
Stack steam inlet partial pressure	65,078.9 Pa
Stack hydrogen inlet partial pressure	38,220.9 Pa
Stack oxygen inlet partial pressure	31,506.44 Pa
Stack steam inlet mole flow rate	0.2051 mol/s
Stack hydrogen inlet mole flow rate	0.0228 mol/s
Stack nitrogen inlet mole flow rate	0.1521 mol/s
Stack oxygen inlet mole flow rate	0.0404 mol/s
Total Voltage	1000.74 V
Calculated Current (<500 s)	29.98 A
Stack inlet temperature (>600 s)	963.9 K
Stack outlet temperature (>600 s)	1063.2 K
Calculated current (>600 s)	39.97 A

11. Scaling Ratio Determination

The objective of this section is to determine the projected case's initial and boundary conditions and transient data based on scaling objectives. For the initial and boundary conditions, the values are implemented into the TEDS and HTSE Dymola systems control to replicate projected-case simulations. In Section 12, the simulation results and projected transient data are compared to assess the scaling performance conducted. The scaling objective is to (1) accelerate TEDS and HTSE test cases introduced in Section 10, (2) match the amount of heat charge and discharge in the TTSS of TEDS, (3) increase the hydrogen production rate to achieve the same overall hydrogen-production load, and (4) perform these simulations without changing instrument type, structure materials, or geometry. To begin this process, the most restrictive system between TEDS and HTSE Dymola models must be determined to decide which scaled equation ratio should be calculated first. After numerous considerations and attempts to change system-control settings for TEDS and HTSE, it was discovered that the TEDS's thermal transport fluid, Therminol-66, was most constrictive when trying to set fluid temperatures higher than 673 K. As TEDS equations modeled in Dymola are written for single phase flow, the hot-side operating temperatures of over 673 K at 1.8 bar triggers a phase change. The gas properties of Therminol-66 are not provided and will break the simulation. While providing a 5 K margin for simulation-solution stability, the upper hot-side temperature limit is 668 K. This upper limit acts as a hard restriction to the TEDS scaling analysis because the maximum heat stored in the TTSS is now finite. If the amount of stored heat is to be matched, the test-case maximum heat storage must be known and can be calculated using the applied mass-flow rate, time of heat-charge mode, specific heat capacity, and the corresponding storage temperature. The total test-case heat storage is 662 MJ at an operating temperature of 598 K. Considering the test-case total heat storage, test-case mass of Therminol-66 fluid in TTSS, and the upper limit operation temperature of 668 K, the target upper-limit mass for the projected case is 3361 kg compared to the test-case mass of 4158 kg. This is the result of following the scaling objective to match total heat storage. Abiding with the scaling objectives and scaled equations for TEDS in Section 8.3, the ω-strain ($\lambda_{A,th} = 1$) coordinate-transformation scaled form from [11] is applicable, and the results are the following:

$$t_R = \left[\frac{k}{\rho_{th} c_{P,th} T_{th,0}}\right]_R, \quad \lambda_{B,th} = \frac{1}{t_R}, \quad \lambda_{A,in} = \left[\frac{c_{P,in} T_{th,0}}{c_{P,th} T_{in,0}}\right]_R, \quad \lambda_{A,out} = \left[\frac{c_{P,out} T_{th,0}}{c_{P,th} T_{out,0}}\right]_R, \quad \lambda_{T_w} = \left[\frac{1}{T_{w,0}}\right]_R \tag{103}$$

Because the test-case and projected-case operating temperatures are known, the maximum accelerated time ratio is 0.855. In addition, because the mass ratio is $3361/4158 = 0.808$, the mass-flow rate ratio is $\dot{m}_R = 0.946$. For the given scaling ratios in Equation (103), the calculated values are $\lambda_{B,th} = 1.219$, $\lambda_{A,in} = 1.000$, $\lambda_{A,out} = 0.996$, and $\lambda_{A,T_w} = 0.959$. To consider the amount of heat supplied by the shell-and-tube heat exchanger (the Chromalox heater in TEDS), the overall heat transfer can be calculated by using the mass-flow rate, total heat-transfer time, specific heat capacity, and temperature difference. Assuming the cold-side temperature is maintained at 498 K, as was true for the test case, the overall heat-transfer ratio is 1.304, which yields an average power of 228.129 kW and maximum power of 260.719 kW for the projected case.

For the HTSE system, the total amount of hydrogen must be conserved. This can be reflected in the established scaled equations in Section 8.4 by enforcing the ω-strain coordinate transformation (details of this type of scaling can be found in [18]) to stack current ($\lambda_{A,I} = 1$) and stack voltage ($\lambda_{A,V}$). This simplifies Equations (77) and (78) to derive the stack average-temperature parameter-of-interest scaling form and nominal stack-voltage ratio as:

$$\lambda_{A,\bar{T}} = \left[\frac{V_0}{\bar{T}_0}\right]_R, \quad V_{0,R} = \left[I\bar{T}_0 e^{\frac{10,300}{\bar{T}}}\right]_R \tag{104}$$

Using the stack-voltage and heat-capacity differential-temperature scaled equation in Equation (80), applied ω-strain coordinate transformation, and scaling objectives to keep

the geometry unchanged, the time ratio can be expressed in terms of SOEC equivalent heat capacity and stack current:

$$t_R = \left[\frac{C_{P,SOEC}}{I}\right]_R \tag{105}$$

Considering the time ratio is determined from TEDS scaling analysis, and the change in heat capacity is minimal compared to stack current changes, the stack current can be approximated to be inversely proportional to the time ratio ($I_R \propto 1/t_R$). Assuming the change in heat capacity accounts for 10% of the stack current change for the given SOEC average-temperature ranges, the stack-current scaling ratio is $I_R = 1.287$. Because the cathode- and anode-feed factors are maintained to be the same (this is to ensure that the balance between supply and consumption is untouched), the inlet-flow-rate scaling ratio for steam, hydrogen, oxygen, and nitrogen is equivalent to the stack-current scaling ratio:

$$w_{H_2O,R} = w_{H_2,R} = w_{O_2,R} = w_{N_2,R} = I_R \tag{106}$$

From Equation (79), the activation overvoltage contribution for stack voltage and stack average temperature is provided. However, it was later determined in Equation (104) that the stack average-temperature parameter-of-interest scaling ratio is $\lambda_{A,\bar{T}} = [V_0/\bar{T}_0]_R$. For both equations to be equivalent, the ratio of the hyperbolic sine must be 1 ($[\sinh(I/2I_{ex,ca})]_R = 1$). To ensure this is always true, the cathode exchange-current scaling ratio is equal to the stack-current ratio ($I_{ex,ca,R} = I_R$). From Equation (47), the cathode-exchange current is given. For the cathode-exchange current-scaling ratio of 1.287, the corresponding stack average temperature is 1079.300 K. Considering the test-case operating-stack average temperature is 1063.150 K, the nominal stack average temperature-scaling ratio is 1.015. Now that the stack current and nominal stack average temperature-scaling ratios are known, the nominal stack-voltage scaling ratio is 1.130. Using the nominal stack-voltage scaling ratio, nominal stack average-temperature scaling ratio, and Equation (104), the stack average-temperature parameter-of-interest scaling ratio is 1.113. For the remaining scaling ratios, some can be determined by considering operational conditions. Throughout the HTSE startup transient and steady-state operation, the SOEC inlet temperature, preheater-inlet steam temperature, and ambient temperature are constant. Thus, the parameter-of-interest scaling ratios are 1 ($\lambda_{A,T_{in}} = \lambda_{A,steam} = \lambda_{amb} = 1$). Using the equations provided and calculated scaling ratios, the rest of the scaled ratios can be calculated, but are omitted due to their having no relevance in the current HTSE Dymola-model variable library.

12. Results and Discussion

For the purpose of this research, it is essential to have the following two components: (1) a test-case simulation, as shown in Section 10, and (2) a scaled case simulation based on the initial and boundary conditions determined in Section 11. In essence, the scaling process is recursive, to converge to the optimal set of scaling equations. The scaling-ratio determination shown in Section 11 is, by definition, a preliminary scaling analysis solely based on feedback from the test-case data. A scaled case simulation using the preliminary scaling analysis acts as a reference to evaluate scaling performance. To investigate the scaling conclusions determined in Sections 8 and 11, Sections 12.1 and 12.2 provide visual evidence for TEDS and HTSE. For the measurement of scaling distortions, the general DSS local separations are calculated using Equation (107):

$$\eta_k = \beta_{P,k}\sqrt{\varepsilon D_{P,k}}\left(\frac{1}{\tilde{\Omega}_{P,k}} - \frac{\lambda_A}{\tilde{\Omega}_{M,k}}\right) \tag{107}$$

where ε is a sign adjuster to ensure the sign within the square-root is always positive. The subscript $k = 1, 2, ..., N$ denotes the transient temporal location of interest (recall, the subscripts M and P are for model and prototype). It should be noted that the corresponding model time location for the given k is not necessarily equivalent to the prototype. If the

scaling case's time ratio is not 1, then it is not equivalent. The coupled model and prototype time is determined by the time ratio (e.g., if $t_R = 0.5$ for prototype time at $t = 1.0$ (s), Equation (107) should be evaluated at $t = 0.5$ (s) for the model). Each temporal location separation provides insights on the distribution of scaling distortions and acts as the qualitative criteria to evaluate scaling performance. Due to the preliminary nature of the scaling analysis, the quantitative criteria is absent and will be addressed in future work. The strategy for defining the quantitative criteria will be comparisons of DSS standard error among different applied scaling decisions. The DSS standard error is the global representation of the local scaling distortions and is shown in Equation (108):

$$\sigma_{DSS} = \sqrt{\frac{1}{N}\sum_{k=1}^{N}(\eta_k^2)} \tag{108}$$

Essentially, the decreased DSS standard error will indicate improvements based on newly applied scaling decisions and vice versa.

12.1. TEDS Scaled Case

As stated in Section 11, the scaling objective is to preserve the physical amount of heat stored at the end of the TTSS charging mode. Considering the increase in maximum heat generation to 260.719 kW from the Chromalox heater, decreased mass-flow rate, and loop cold-side maintained at 498 K (same as the test case in Section 10), the charge- and discharge-mode simulations were conducted and are shown in Figures 15a,b and 16a,b. Starting from the charge-mode comparison, the anticipated maximum temperature increase from 598 K to 668 K is reflected. Note that the starting temperature is 498 K, which is common between test and scaled cases. The increased temperature difference preserves the amount of TTSS heat storage as the scaled TTSS injected hot-fluid mass is reduced to approximately 80% of the test case. This explains the reduction in charge-outlet temperature increase as the TTSS is only a relative fraction of the test case, and not enough time has elapsed to transport hot-line Therminol-66 fluid to the TTSS charge-outlet line. Because the discharge inlet pulls Therminol-66 from the cold line, the temperature remains at 498 K.

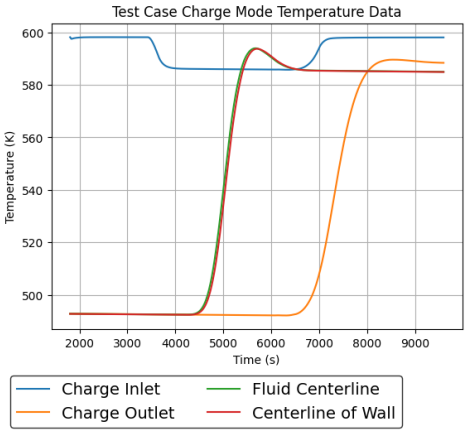

(**a**) Test-case core parameters to evaluate the TTSS charge mode.

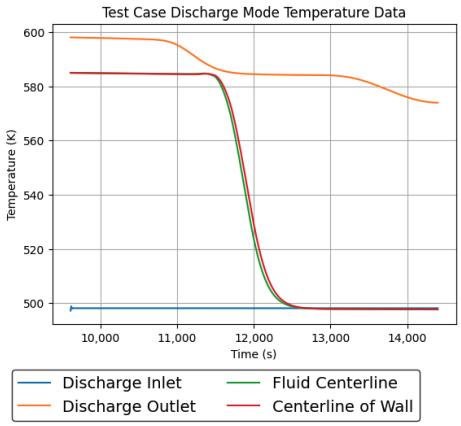

(**b**) Test-case core parameters to evaluate the TTSS discharge mode.

Figure 15. Test-case time-dependent thermal distribution for charge and discharge mode. Includes the TTSS inlet, outlet, centerline, and wall-centerline temperatures.

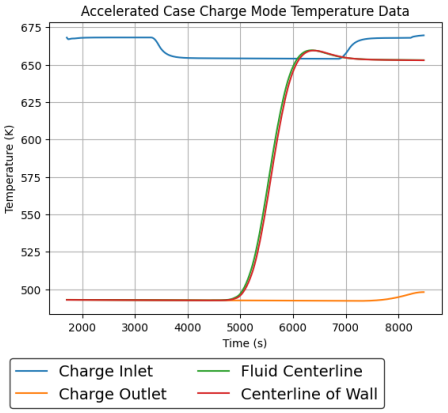

(**a**) Scaled-case core parameters to evaluate the TTSS charge mode.

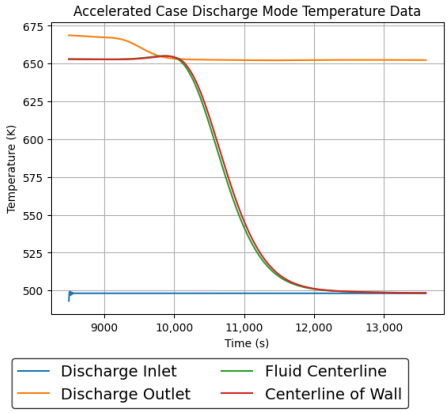

(**b**) Scaled-case core parameters to evaluate the TTSS discharge mode.

Figure 16. Scaled-case time-dependent thermal distribution for the charge and discharge mode. Includes TTSS inlet, outlet, centerline, and wall-centerline temperatures.

The steps to calculate the DSS projected data are to (1) determine the time ratio, (2) determine the parameter-of-interest scaling ratio (λ_A), and (3) use Equation (8) to post-process test-case data. Reorganizing Equation (8) and plugging in Equation (1) gives the relation to calculate the projected data, given the prototypical system, for the test case:

$$\Psi = \Psi_0 \beta_{projected} = \Psi_0 \beta_{test} \lambda_A \tag{109}$$

Following the defined steps and using the preliminary scaling analysis, the projected case data were calculated for the TSS inlet, outlet, centerline, and wall-centerline temperatures; these are shown in Figure 17a,b. From the first look, the charge-outlet, discharge-inlet, discharge-outlet, charge-centerline, discharge-centerline, wall-charge, and wall-discharge temperatures show different features. For the charge-centerline, charge-wall, and all discharge temperatures, the timing and magnitude are offset. For the charge-outlet temperature, the data geometry indicates a large temperature increase after 5500 s, starting from 403 K. This behavior can be explained by considering that all variables were normalized by the corresponding temperature values at the end of the charge mode (for the projected case around 9596.167 s and for the scaled case around 8477.034 s). The definition to be normalized is to adjust magnitudes that range around 1. The issue is the low temperature value relative to the reference value.

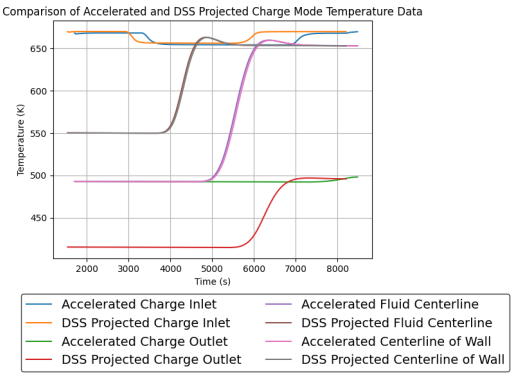

(**a**) Comparison of projected- and scaled-case charge-mode core parameters.

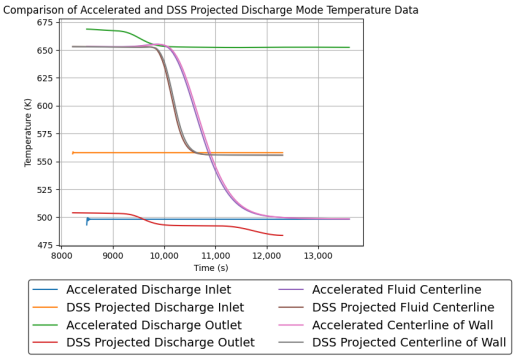

(**b**) Comparison of projected- and scaled-case discharge-mode core parameters.

Figure 17. Comparison of projected- and scaled-case time-dependent thermal distribution for charge and discharge modes. Includes TTSS inlet, outlet, centerline, and wall-centerline temperatures.

For example, consider the normalization at the initial charge time for both cases. For the scaled case, the reference temperatures are 668, 500, and 650 K for the charge inlet, charge outlet, and centerline temperatures, respectively, which correspond to normalized values of 1.000, 0.991, and 0.842. For the test case (recall Equation (109)), the reference temperatures are 668, 582, and 581 K, which correspond to normalized values of 1.000, 0.841, and 0.755, respectively. The difference in normalized values is mainly due to the relative magnitude of cold-side temperatures. As hot-side temperatures were upscaled, the cold-side temperatures remained the same, causing lower-temperature normalized values to differ significantly. Although from the scaling standpoint, such decisions lead to scaling distortions, for operations, it is standard. If the cold-side temperatures were upscaled, this would suggest that the TTSS was precharged before the event and would not represent a case where the system is charged with the specified heat-storage amount. This adds complications because the parameter-of-interest scaling ratio for thermal terms is approximately 1 and, when applying Equation (109), the normalized values from the test case are inherited, outputting higher temperatures than were observed from the scaled case.

As mentioned earlier, scaling analyses are recursive and are subject to modifications when less-compatible scaling decisions are made. In this case, the combination to normalize by the chosen reference value and leave the cold-line temperatures resulted in distorted projections. Furthermore, although it may not be obvious, the discharge projected case, in terms of data geometry, performed better than the charge projected case. This suggests that there should be a separate scaling for charge and discharge modes. To modify the scaling analysis to account for the low temperatures and varied scaling performance between both operational modes, it is suggested that the normalizing method be changed. Regardless of what reference value is used—whether it is a temperature value at some time or the temperature difference—the unscaled lower temperatures always trigger scaling distortions. One normalizing method that is capable of considering both maximum and minimum values is the minmax scaler used in machine learning. This is shown in Equation (110).

$$T^{+} = \frac{T - T_{min}}{T_{max} - T_{min}} \tag{110}$$

Essentially, each data point is resized to range from 0 to 1 where 0 is at the minimum value and 1 is at the maximum value.

When applying the minmax scale, Figure 18a,b show the difference when considering the minimum and maximum values, regardless of temporal location. Magnitudes are now adjusted to be roughly the same, and this is the correct normalization method for the type of assumptions and scaling decisions imposed. Because it was identified. based on Figure 17a,b, that the necessity to separate scaling analyses among charge and discharge operations was emphasized, different time ratios were applied to achieve the results in Figure 18a,b. One remaining shortcoming from the modified scaling analysis is the different transient trends observed at certain time intervals for the charge and discharge modes. For the charge mode, between 4000 and 6000 s and 6500 and 8100 s for centerline and charge-outlet temperatures were observed. For the discharge mode, between 9300 and 12,500 s and 10,300 and 12,200 s for discharge-outlet and centerline temperatures were found. The root cause of these distortions is inadequacies modeling the scaled conditions defined in Section 11. Figure 19a,b show the test- and scaled-case mass-flow rates. Immediately, it can be seen that the control sequences between the test and scaled cases are different. Regardless of a change to the timing by a time ratio of 0.855, the on, off, ramping up, and ramping down do not behave as planned. This results in different fluid-injection and ejection sequences, altering the data geometry and trends.

Another aspect that supports the conclusion of a mal-control sequence in the scaled Dymola simulation is the measured separation for inlet, outlet, fluid centerline, and wall centerline temperatures shown in Figures 20a,b and 21a,b. It can be shown that relatively high separations are observed around the charge to discharge mode transition, which suggests the heater and mass flow rate controls were not optimal enough to represent the

defined scaled-case. Moreover, the initial 1000 s of the charge inlet temperature exhibit unexpected distortions that are possibly rooted from the previously stated issue but will require further investigations to comprehend the source of the anomaly For future references, an improved understanding of the system controls in the Dymola TEDS model is required for better scaling validations concerning the control of heaters and the mass flow rate approaching and after the transition from charge to discharge mode. Overall, the charge mode temperatures show larger distributions of distortions than the discharge mode.

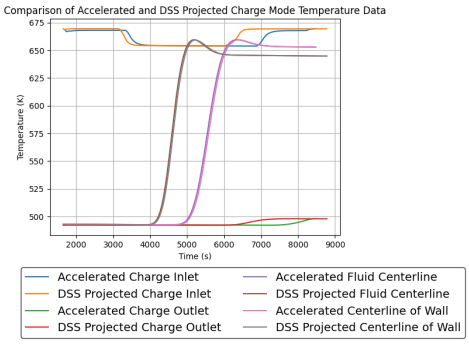

(**a**) Comparison of the modified projected- and scaled-case charge-mode core parameters.

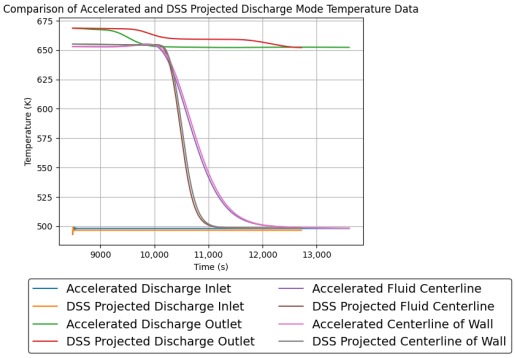

(**b**) Comparison of the modified projected- and scaled-case discharge-mode core parameters.

Figure 18. Comparison of the modified projected- and scaled-case time-dependent thermal distribution for charge and discharge modes. Includes TTSS inlet, outlet, centerline, and wall-centerline temperatures.

To emphasize the importance of the stated findings, consider an IES case where the stored heat is discharged for chemical processing. Chemical process plants are hard conditioned systems that can only operate with specific temperature, pressure, and other conditions dependent on the given process. If the heat from thermal energy systems is used, precise system controls are required to ensure operating conditions are constantly met, even when transitioning from one heat source to another. The findings based on the scaling analysis applied amplify the control issues found in the scaled Dymola case. Without the scaling analysis, there would be difficulties on justifying the bridge between one case with the other and determining which transients require improvements. By having the capability to project data from test cases, the ideal behavior based on the governing equations, scaling theory, and selected assumptions can be obtained and, to a certain degree, avoid costly retroactive facility changes as identified issues addressed during the pre-design phase. The recursive process of refining the scaling analysis will guarantee the validity, and the current analysis is the first iteration to achieve this goal.

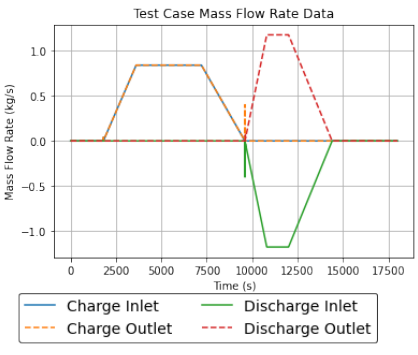

(**a**) Test-case mass-flow rate control.

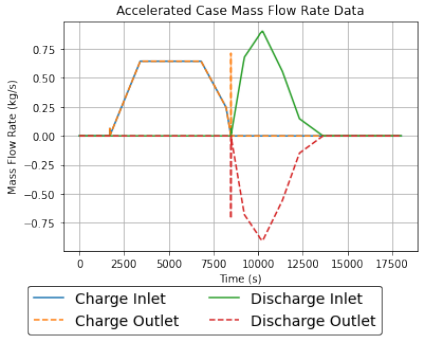

(**b**) Scaled-case mass-flow rate control.

Figure 19. Test- and scaled-case time-dependent mass-flow rate control.

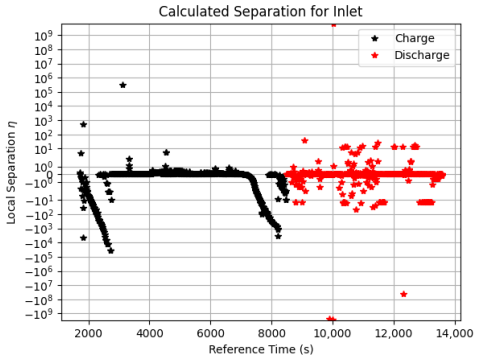

(**a**) Charge and discharge inlet temperature measured local scaling distortions.

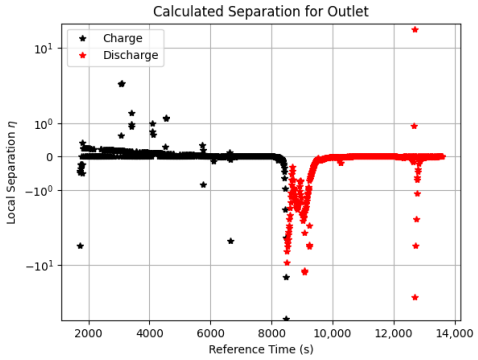

(**b**) Charge and discharge outlet temperature measured local scaling distortions.

Figure 20. Inlet and outlet temperature measured local scaling distortions.

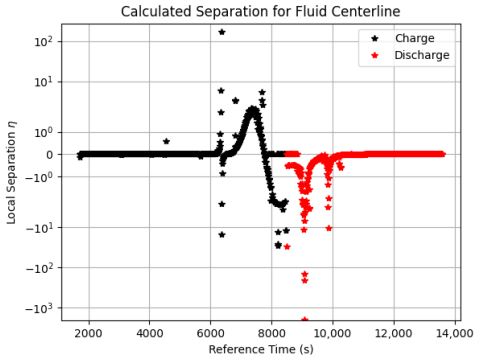

(**a**) Thermocline fluid centerline mid-height temperature measured local scaling distortions.

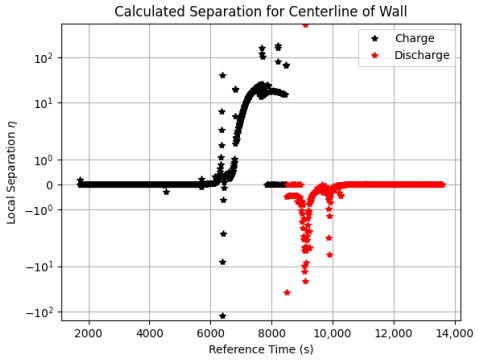

(**b**) Thermocline wall centerline mid-height temperature measured local scaling distortions.

Figure 21. Thermocline temperature measured local scaling distortions.

12.2. HTSE

For HTSE, the scaling objective is to increase hydrogen production by adjusting the stack current, voltage, and average temperature. Considering the 1.28 factor increase in stack current, 1.23 factor increase in voltage per cell, and significant increase in the stack average temperature to 1201.270 K, inlet mass-flow rates of 0.264 mol/s, 0.0293 mol/s, and 0.0520 mol/s for steam, hydrogen, and oxygen were determined. Assuming the area-specific resistance remains unchanged, Table 7 shows the results of the scaled case HTSE simulation. As stated in Section 10.2.2, the HTSE simulation is a time-dependent steady-state problem. In reality, the startup of the stack should slowly (over approximately 20 s) increase the applied voltage and furnace temperature until operating conditions are achieved for the specified stack current. Instead, the current Dymola HTSE model inversely solves for the stack current assuming thermal-neutral voltage and cell voltage based on furnace temperatures without delay feedback from the cathode- and anode-stack average pressures. The outcome is steady-state stack voltage and furnace temperature. For the applied scaling performance, the steam-inlet mole-flow rate, hydrogen inlet flow rate, and stack voltage increased as anticipated. However, the projected applied temperatures, oxygen mole-flow rate, nitrogen mole-flow rate, and stack current did not behave as in the scaled-case simulation. Despite increasing the scaled-case stack temperature to 1201 K, the applied temperatures did not increase significantly, and the possibility of mistakenly not reflecting other temperature conditions in other modeled components is high. For the scaled-case nitrogen mole-flow rate, oxygen mole-flow rate, and calculated current, it was

revealed by the Dymola model code that the physics were being calculated differently from the equation set used in Section 7. The modeled current density and stack power are [17]:

$$i = \frac{\text{Operating Voltage} - \text{Open Circuit Voltage}}{ASR}, \qquad \text{Stack Power} = \text{Operating Voltage} \cdot i \cdot A \tag{111}$$

Because the current density is calculated by subtracting the operating voltage from the open circuit voltage, and the area-specific resistance is unchanged by the scaling objectives stated in Section 11. The open-voltage reduced numerator values increase, and as a result, the stack-current decreased compared to the test case values. The corrective action is to either (1) change HTSE scaling equations to adopt Dymola models, or (2) modify the Dymola models to adhere to the set of HTSE equations introduced in Section 7. Although the cathode mole-flow rates were not affected, a significant reduction in anode mole-flow rates was observed. The HTSE findings in this case suggest that the applied scaling analysis was capable of discovering misplaced physics based on the projected results, as simulation model discrepancy is a large source of error. Unfortunately, due to the steady-state transient nature of HTSE Dymola runs, Equation (107) cannot be used to visualize distributions of scaling distortions as DSS post-processed parameters require dynamic behavior. Further investigations on the exact cause will be conducted.

Table 7. Scaled and projected case values of test case. Absolute relative errors are in reference to the projected case values.

Output Parameter	Scaled Case Value	Projected Case Value	Absolute Relative Error (%)
Stack inlet temperature (<500 s)	1006.21 K	1092.68 K	7.91
Stack outlet temperature (<500 s)	1062.72 K	1281.62 K	17.08
Ambient temperature	293.10 K	293.10 K	0.00
Stack steam inlet partial pressure	65,078.9 Pa	65,078.9 Pa	0.00
Stack hydrogen-inlet partial pressure	38,220.9 Pa	38,220.9 Pa	0.00
Stack oxygen-inlet partial pressure	31,506.44 Pa	31,506.44 Pa	0.00
Stack steam-inlet mole-flow rate	0.264 mol/s	0.264 mol/s	0.00
Stack hydrogen-inlet mole-flow rate	0.0293 mol/s	0.0293 mol/s	0.00
Stack nitrogen-inlet mole-flow rate	0.0630 mol/s	0.167 mol/s	62.28
Stack oxygen-inlet mole-flow rate	0.0167 mol/s	0.0520 mol/s	67.89
Total voltage	1131 V	1131 V	
Calculated current (<500 s)	26.53 A	34.14 A	22.28
Stack inlet temperature (>600 s)	973.7 K	1069.9 K	8.99
Stack outlet temperature (>600 s)	1063.2 K	1281.6 K	17.04
Calculated current (>600 s)	35.37 A	51.43 A	31.22

13. Conclusions

In a first attempt to validate scaling activities under the IES program, multiple systems between TEDS and HTSE were scaled, and Dymola test cases were simulated. Based on test-case initial and boundary conditions and scaling objectives, the corresponding scaling ratios to calculate the scaled-case operating conditions and predict scaled-case simulation data were determined. The test-case models were modified accordingly, and the scaled-case models were simulated under the specified operating conditions. Concurrently, the scaled ratios applied to the test- and scaled-case data were predicted (and referred to as the projected-case). After comparing the projected- and scaling-case data, several defects in the TEDS preliminary scaling analysis were discovered, and applied governing-equation discrepancies were identified for the HTSE preliminary scaling analysis. To improve TEDS scaling performance, the normalization method was changed accordingly, and the scaling predictive capabilities were significantly enhanced. For HTSE scaling, two possible corrective actions were recognized; it was determined that further investigations would be required to fully comprehend the extent of the scaling distortions exhibited. The findings, based on measured separation for TEDS inlet, outlet, fluid centerline, and wall centerline temperatures shown in Figures 20a,b and 21a,b, suggest a mal-control sequence of the scaled Dymola simulation reflecting the conditions derived, and relatively high separations are observed around the charge to discharge mode transition. This is of great relevance to the large-scale and actual implementation of IES as precise system controls

are required to ensure optimal coordination during flexible operations. As scaling processes are recursive and potentially require multiple reevaluations in order to converge to the optimal form, studies following this research will attempt to further improve the currently established scaling analysis to achieve facility-demonstration quality. One aspect to note is that the simulations were conducted on TEDS and HTSE separately. Although the intent was to have an integral system simulation to observe the scaling-analysis performance on the integral level, certain incompatibilities between the TEDS and HTSE models existed, delaying code development. In a case in which sufficient modifications are made, the same analysis will be conducted once more. To increase system similarity for TEDS and HTSE, scaling validation via facility demonstration is required. Finally, having the capability to project data from test cases, the ideal behavior based on the governing equations, scaling theory, and selected assumptions can be obtained. For virtual IES emulations between facilities of multiple scales, the demonstrated capabilities can convert system-to-system signals enabling near-realistic IES operations and assist efforts to realize real-world IES.

Author Contributions: Conceptualization, R.Y.; methodology, R.Y. and S.C.; data curation and data analysis, R.Y. and S.C.; supervision, A.E.; resources, A.E.; writing—original draft preparation, R.Y. and S.C.; writing—review and editing, A.E.; project administration, A.E.; funding acquisition, A.E. All authors have read and agreed to the published version of the manuscript.

Funding: This manuscript was funded by Battelle Energy Alliance, LLC, under contract number DE-AC07-05ID14517 with the US Department of Energy. The United States Government retains and the publisher, by accepting the article for publication, acknowledges that the US Government retains a non-exclusive, paid-up, irrevocable, worldwide license to publish or reproduce the published form of this manuscript, or allow others to do so, for US Government purposes.

Institutional Review Board Statement: This document was reviewed under the Peer Review System and Lab Review System of INL to ensure the quality of this document and verification of disclosable data under data-classification regulations.

Data Availability Statement: The data are available within this document. Normalized values and other parameters are provided and are capable of calculating the original dataset.

Acknowledgments: The authors would like to thank the INL IES Program for providing funding for the application of integral system scaling, Terry Morton for providing facility reports, Daniel Mikkelson for decoupling the TEDS-MAGNET Dymola model, Amey Shigrekar for not only developing the HTSE Dymola model but also for providing abundant simulation advice, and Jeremy Hartvigsen and Micah Casteel for providing useful information for steam electrolysis in general.

Conflicts of Interest: The authors declare no conflict of interest. The funders had no role in the design of the study; in the collection, analyses, or interpretation of data; in the writing of the manuscript, or in the decision to publish the results.

Abbreviations

The following abbreviations are used in this manuscript:

BOP	Balance of Plant
DETAIL	Dynamic Energy Transport and Integration Laboratory
DSS	Dynamical System Scaling
FORCE	Framework for Optimization of ResourCes and Economics
INL	Idaho National Laboratory
HX	Heat Exchanger
HTSE	High Temperature Steam Electrolysis
IES	Integrated Energy System
LMTD	Log-Mean Temperature Difference
MTD	Mean Temperature Difference
NPP	Nuclear Power Plant

NREL	National Renewable Energy Laboratory
PID	Proportional – Integral – Derivative
SOEC	Solid-Oxide Electrolysis
TEDS	Thermal Energy Distribution System
TTSS	Thermocline Thermal Storage System

References

1. Morton, T.J. Integrated Energy Systems Experimental Systems Development. United States Department of Energy. 2020. Available online: https://www.osti.gov/servlets/purl/1668842 (accessed on 10 March 2022).
2. Levin, T.; Botterud, A.; Mann, W.N.; Kwon, J.; Zhou, Z. Extreme Weather and Electricity Markets: Key Lessons from the February 2021 Texas Crisis. *Joule* **2022**, *6*, 1–7. [CrossRef]
3. Eliana, R. Argentina Capital Hit by Major Power Outage Amid Heat Wave. News Article: Reuters. 11 January 2022. Available online: https://www.reuters.com/world/americas/argentina-capital-hit-by-major-power-outage-amid-heat-wave-2022-01-11/ (accessed on 31 May 2022).
4. Ma, J.; Li, L.; Wang, M.; Du, Y.; Ma, J.; Zhang, X.; Wang, Z. Carbon Capture and Storage: History and the Road Ahead. *Engineering* **2022**, *14*, 33–43. [CrossRef]
5. Bragg-Sitton, S.M. *Next Generation Nuclear Energy: Advanced Reactors and Integrated Energy Systems*; U.S. Department of Energy, Office of Scientific and Technical Information: Washington, DC, USA, 2022. Available online: https://www.osti.gov/servlets/purl/1865609 (accessed on 31 May 2022).
6. Epiney, A.S.; Talbot, P.W.; Saeed, R.M.; Wendt, D.S.; Garrett, D.; Abdo, M.M.; Yoshiura, R.K.; Yoo, J.S.; Mikkelson, D.M.; Hansen, J.K.; et al. *Roadmap for IES Modeling and Simulation Activities*; U.S. Department of Energy, Office of Scientific and Technical Information: Washington, DC, USA, 2022. Available online: https://www.osti.gov/biblio/1973466 (accessed on 22 June 2023).
7. Saeed, R.M.; Shigrekar, A.; Mikkelson, D.M.; Rigby, G.; Christopher, A.; Hui, Y.; Otani, C.M.; Garrouste, M.; Frick, K.L.; Bragg-Sitton, S.M. *Multilevel Analysis, Design, and Modeling of Coupling Advanced Nuclear Reactors and Thermal Energy Storage in an Integrated Energy System*; U.S. Department of Energy, Office of Scientific and Technical Information: Washington, DC, USA, 2022. [CrossRef]
8. Mikkelson, D.M.; Frick, K.; Bragg-Sitton, S.M.; Doster, J.M.; Worsham, E.K. *Thermal Energy Storage Selection for Near Term Nuclear Integration*; U.S. Department of Energy, Office of Scientific and Technical Information: Washington, DC, USA, 2019. [CrossRef]
9. McFly, S.; Peterson, J.; Cryar, R.; Reynolds, T. *Distributed Energy Resource Visual Emulator: Phase 1*; U.S. Department of Energy, Office of Scientific and Technical Information: Washington, DC, USA, 2023. [CrossRef]
10. Bragg-Sitton, S.M.; Rabiti, C.; Boardman, R.; O'Brien, J.; Morton, T.; Yoon, S.; Yoo, J.; Sabharwall, P.; Harrison, T.; Greenwood, M.; et al. *Integrated Energy Systems: 2020 Roadmap*; U.S. Department of Energy, Office of Scientific and Technical Information: Washington, DC, USA, 2020. [CrossRef]
11. Yoshiura, R.K.; Duenas, A.M.; Epiney, A.S. Dynamical System Scaling of a Thermocline Thermal Storage System in the Thermal Energy Distribution System (TEDS) Facility. *Energies* **2022**, *15*, 4265. [CrossRef]
12. Yoshiura, R.K.; Fishler, J.D.; Epiney, A.S.; Ketrow, Z. *DETAIL Component Scaling and Methodology Comparison*; INL/RPT-22-69180-Rev000; Idaho National Laboratory: Idaho Falls, ID, USA, 2021. Available online: https://www.osti.gov/biblio/1892319 (accessed on 22 June 2023).
13. Frick, K.L.; Alfonsi, A.; Rabiti, C.; Mikkelson, D.M. *Hybrid User Manual*; INL/MIS-20-60624-Rev001; Idaho National Laboratory: Idaho Falls, ID, USA, 2021. Available online: https://www.osti.gov/biblio/1863262 (accessed on 22 June 2023).
14. Brück, D. Dymola Referential. 12 April 2023. Available online: https://www.3ds.com/fileadmin/PRODUCTS/CATIA/DYMOLA/PDF/Dymola-referential-2023.pdf (accessed on 22 June 2023).
15. The Modelica Association. Modelica Language. 2000–2021. Available online: https://modelica.org/modelicalanguage.html (accessed on 22 June 2023).
16. Frick, K.; Bragg-Sitton, S.; Rabiti, C. Modeling the Idaho National Laboratory Thermal-Energy Distribution System (TEDS) in the Modelica Ecosystem. *Energies* **2020**, *13*, 6353. [CrossRef]
17. Mikkelson, D.M.; Shigrekar, A.; Epiney, A.S.; Ho, A.; Greenwood, S.; Frick, K.L. *HYBRID Modeling of the DETAIL Experimental Facility*; INL/EXT-22-02188-Rev001; Idaho National Laboratory: Idaho Falls, ID, USA, 2022. [CrossRef]
18. Reyes, J.N. The Dynamical System Scaling Methodology. In Proceedings of the 16th International Topical Meeting on Nuclear Thermal Hydraulics, Chicago, IL, USA, 30 August–4 September 2015.
19. Reyes, J.N.; Frepoli, C.; Yurko, J.P. The Dynamical System Scaling Methodology: Comparing Dimensionless Governing Equations with the H2TS and FSA Methodologies. In Proceedings of the 16th International Topical Meeting on Nuclear Thermal Hydraulics, Chicago, IL, USA, 30 August–4 September 2015.
20. Marting, R.P.; Frepoli, C. *Design-Basis Accident Analysis Methods for Light-Water Nuclear Power Plants*, 1st ed.; World Scientific: Singapore, 2019; pp. 181–263. [CrossRef]
21. Einstein, A.; Infeld, L. *The Evolution of Physics from Early Concepts to Relativity and Quanta*, 1st ed.; Simon and Schuster Publisher: New York, NY, USA, 1966. [CrossRef]
22. Yoshiura, R.K. Dynamic System Scaling Application to Accelerated Nuclear Fuel Testing. In Proceedings of the 19th International Topical Meeting on Nuclear Thermal Hydraulics, Brussels, Belgium, 6–11 March 2022.

23. Gunn, D.J. Transfer of heat or mass to particles in fixed and fluidised beds. *Int. J. Heat Transf.* **1978**, *21*, 467. [CrossRef]
24. Esence, T.; Brunch, A.; Molina, S.; Stutz, B.; Fourmigue, J.F. A review on experience feedback and numerical modeling of packed-bed thermal energy storage systems. *Sol. Energy* **2017**, *153*, 628–654. [CrossRef]
25. Xing, X.; Lin, J.; Song, Y.; Hu, Q.; Zhou, Y.; Mu, S. Optimization of hydrogen yield of a high-temperature electrolysis system with coordinated temperature and feed factors at various loading conditions: A model-based study. *Appl. Energy* **2018**, *232*, 368–385. [CrossRef]
26. Xing, X.; Lin, J.; Song, Y.; Hu, Q. Maximum Production Point Tracking of a High-Temperature Power-to-Gas System: A Dynamic-Model-Based Study. *IEEE Trans. Sustain. Energy* **2020**, *11*, 361–370. [CrossRef]
27. Elder, R.; Cumming, D.; Mogensen, M. Chapter 11—High Temperature Electrolysis. In *Carbon Dioxide Utilisation*; Elsevier Science: Amsterdam, The Netherlands, 2015; pp. 183–209. [CrossRef]
28. Amphlett, J.; Baumert, R.; Mann, R.; Peppley, B.; Roberge, P.; Harris, T. Performance Modeling of the Ballard Mark IV Solid Polymer Electrolyte Fuel Cell: I. Mechanistic Model Development. *J. Electrochem. Soc.* **1995**, *142*, 1–9. [CrossRef]
29. O'Brien, J.; McKellar, M.; Harvego, E.; Stoots, C. High-temperature electrolysis for large-scale hydrogen and syngas production from nuclear energy—Summary of system simulation and economic analyses. *Int. J. Hydrogen Energy* **2010**, *35*, 4808–4819. [CrossRef]
30. Frick, K.L.; Bragg-Sitton, S.M.; Cristian, R.; Andrea, A. *Development of the IES Plug-and-Play Framework*; INL/EXT-21-62050-Rev001; Idaho National Laboratory: Idaho Falls, ID, USA, 2021. [CrossRef]
31. Frick, K.; Bragg-Sitton, S.; Garrouste, M. *Validation and Verification Methodology for INL Modelica-Based TEDS Models via Experimental Results*; INL EXT-21-64408-Rev000; Idaho National Laboratory: Idaho Falls, ID, USA, 2021. [CrossRef]
32. Frick, K.L.; Bragg-Sitton, S.M.; Cristian, R. *Development of the INL Thermal Energy Distribution System (TEDS) in the Modelica Eco-System for Validation and Verification*; INL/EXT-20-59195; Idaho National Laboratory: Idaho Falls, ID, USA, 2020. [CrossRef]
33. Van Lew, J.T.; Li, P.; Chan, C.L.; Karaki, W.; Stephens, J. Analysis of Heat Storage and Delivery of a Thermocline Tank Having Solid Filler Material. *J. Sol. Energy Eng.* **2011**, *133*, 021003. [CrossRef]